J. Fluid Mech. (2023), *vol*. 966, A45, doi:10.1017/jfm.2023.470

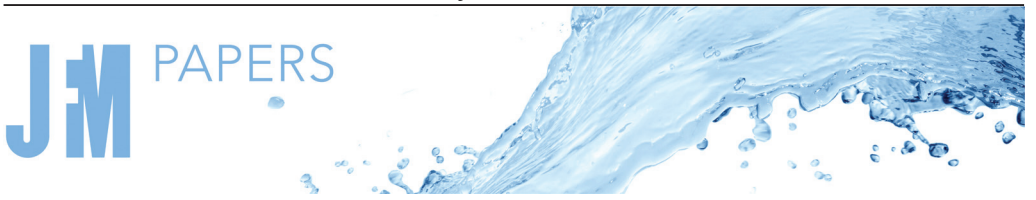

Slow-growth approximation for near-wall patch representation of wall-bounded turbulence

Sean P. Carney[1],† **and Robert D. Moser**[2,3]

[1]Department of Mathematics, University of California, Los Angeles, CA 90095, USA

[2]Oden Institute for Computational Engineering and Sciences, The University of Texas at Austin, TX 78712, USA

[3]Department of Mechanical Engineering, The University of Texas at Austin, TX 78712, USA

(Received 17 October 2022; revised 29 April 2023; accepted 29 May 2023)

Wall-bounded turbulent shear flows are known to exhibit universal small-scale dynamics that are modulated by large-scale flow structures. Strong pressure gradients complicate this characterization, however. They can cause significant variation of the mean flow in the streamwise direction. For such situations, we perform asymptotic analysis of the Navier–Stokes equations to inform a model for the effect of mean flow growth on near-wall turbulence in a small domain localized to the boundary. The asymptotics are valid whenever the viscous length scale is small relative to the length scale over which the mean flow varies. To ensure the correct momentum environment, a dynamic procedure is introduced that accounts for the additional sources of mean momentum flux through the upper domain boundary arising from the asymptotic terms. Comparisons of the model's low-order, single-point statistics with those from direct numerical simulation and well-resolved large eddy simulation of adverse-pressure-gradient turbulent boundary layers indicate the asymptotic model successfully accounts for the effect of boundary layer growth on the small-scale near-wall turbulence.

Key words: turbulent boundary layers, turbulence simulation, boundary layer structure

1. Introduction

High-Reynolds-number wall-bounded turbulent shear flows are characterized by a separation of scales between the flow in the near-wall region, in which mean viscous stresses play an important role, and the flow farther away from the wall, where mean viscous effects are negligible. The friction Reynolds number $Re_\tau = \delta/\delta_\nu$ quantifies this separation of scales, where δ is the characteristic length scale of the shear layer, such as

† Email address for correspondence: spcarney@math.ucla.edu

a channel half-width, a pipe radius or a boundary layer thickness, and $\delta_\nu = \nu/u_\tau$ is the viscous length scale, where ν is the kinematic viscosity of the fluid, $u_\tau = \sqrt{\tau_w/\rho}$, τ_w is the mean wall shear stress and ρ is the fluid density. To simulate all the scales of motion in a wall-bounded flow requires $O(Re_\tau^{2.5})$ and $O(Re_\tau^2)$ spatial degrees of freedom for direct numerical simulation (DNS) and large eddy simulation (LES), respectively (Mizuno & Jiménez 2013). Even on modern high-performance computing systems, this cost is prohibitively large for important atmospheric and aeronautical flows, for example, which routinely occur at $10^4 \lesssim Re_\tau \lesssim 10^7$ (Smits & Marusic 2013). Developing reduced order models, such as wall-modelled LES, to overcome this challenge requires an understanding of the mutual interactions between small- and large-scale motions in the outer and near-wall regions.

Advances in computational power and experimental techniques have enabled a great deal of insight into the inner/outer interactions for the canonical zero-pressure gradient boundary layer and fully developed pipe and channel flows (Smits, McKeon & Marusic 2011). It is well established that there is an autonomous near-wall cycle of self-sustaining mechanisms (Jiménez & Moin 1991; Hamilton, Kim & Waleffe 1995; Jeong *et al.* 1997), involving low and high speed streamwise velocity streaks and coherent structures of quasi-streamwise vorticity. Jiménez & Pinelli (1999) showed that this cycle of near-wall dynamics persists without any input from the turbulence farther away from the wall. Large-scale motions, or superstructures, in the outer layer do indeed impact the near-wall region, however. They modulate the turbulent velocity fluctuations and superimpose their energy (Hutchins & Marusic 2007; Marusic, Mathis & Hutchins 2010*a*; Ganapathisubramani *et al.* 2012), and their influence increases with Re_τ (DeGraaff & Eaton 2000). Spectral analysis of both channel (Lee & Moser 2019; Wang, Hu & Zheng 2021*b*) and boundary layer flow data (Samie *et al.* 2018) has demonstrated that, in contrast, the dynamics of the small-scale motions in the near-wall region are universal. The small-scale, high-wavenumber energy, as well as its production, dissipation and transport, are independent of Re_τ.

Based on this characterization of near-wall dynamics, Carney, Engquist & Moser (2020) formulated numerical simulations on near-wall 'patch' (NWP) domains whose size scaled in viscous units. Similar to the numerical experiments of Jiménez & Moin (1991) and Jiménez & Pinelli (1999), the model used restricted domain sizes and, as in the latter, manipulation of the turbulence outside of the near-wall region to simulate only the autonomous dynamics over the range of scales at which they occur. The model reproduced near-wall small-scale statistics obtained from DNS, confirming that the 'universal signal' described by Marusic, Mathis & Hutchins (2010*b*) and Mathis, Hutchins & Marusic (2011) indeed arises from universal dynamics, independent of Re_τ or external flow configuration. As a computational model, the NWP defined a one-parameter family of turbulent flows parameterized by the near-wall, viscous-scaled pressure gradient. Because of its ability to reproduce a variety of well-known features of high Re_τ wall turbulence at a computational cost that is orders of magnitude less than DNS, the model offers a way to efficiently probe the response of near-wall turbulence to changes in the mean momentum environment.

The NWP model was validated against DNS data from channel flows, featuring mild favourable pressure gradients, and a zero-pressure-gradient (ZPG) boundary layer. Because of their relevance to engineering applications, it is reasonable to ask if the NWP model can adequately describe the near-wall, small-scale dynamics of flows with adverse pressure gradients (APGs), especially APG boundary layers. Although the understanding of scale interactions between inner and outer regions in APG boundary layers is less complete than for ZPG flows, there has been much progress since the early experimental

studies of Clauser (1954) and Bradshaw (1967) and numerical simulations of Spalart & Leonard (1987) and Spalart & Watmuff (1993); see also references therein. More recent experimental investigations include the works of Rahgozar & Maciel (2012), Harun *et al.* (2013), Knopp *et al.* (2015), Knopp *et al.* (2017), Sanmiguel Vila *et al.* (2017, 2020) and Romero *et al.* (2022). Previous large-scale simulations include DNS (Na & Moin 1998; Skote & Henningson 2002; Gungor *et al.* 2016) and well-resolved LES (Hickel & Adams 2008) of separated boundary flows and a separated channel flow (Marquillie, Laval & Dolganov 2008), while large-scale simulations of attached APG boundary layers have been conducted by Lee & Sung (2009), Kitsios *et al.* (2017), Lee (2017) and Yoon, Hwang & Sung (2018) using DNS, as well as by Inoue *et al.* (2013), Bobke *et al.* (2017) and Pozuelo *et al.* (2022) using well-resolved LES. Simulations over complex airfoil geometries have also been performed with both DNS (Hosseini *et al.* 2016) and well-resolved LES (Sato *et al.* 2017; Tanarro, Vinuesa & Schlatter 2020).

One observation that has consistently emerged in the literature is that, even when mild adverse pressure gradients energize the large-scale structures in both the outer layer and the near-wall region of the boundary layer. The increased influence of the large scales also results in increased modulation effects on the small scales (Harun *et al.* 2013; Lee 2017; Yoon *et al.* 2018), analogous to the effect of increasing Re_τ in ZPG boundary layers. Although APGs have been shown to energize the small-scale motions in the outer region of a boundary layer (Sanmiguel Vila *et al.* 2020), less appears to be known about the small-scale energy in the near-wall region. After filtering out contributions from spanwise wavelengths $\lambda_z/\delta_\nu \gtrsim 180$, Lee (2017) found that the small-scale contribution to both the streamwise velocity variance and the Reynolds shear stress increased with pressure gradient, while Sanmiguel Vila *et al.* (2020) found that the small-scale contributions to the streamwise velocity variance from motions with streamwise wavelengths $\lambda_x/\delta_\nu \lesssim 4300$ was independent of the pressure gradient strength. One objective of the current work is to use a near-wall patch computational model to investigate the extent to which the small-scale, near-wall dynamics are responsible for the low order flow statistics of adverse-pressure-gradient flows observed in experiments and large-scale simulations. Since the NWP model simulates only the small-scale motions, isolated from large-scale influences, any differences between its statistical profiles and those from DNS or large-scale simulations can reasonably be attributed to the superposition and modulation effects of the large-scale motions that are missing. In this way, the model is similar to the computational 'experiments' of Jiménez & Moin (1991) and Jiménez & Pinelli (1999) in which near-wall turbulence is artificially manipulated and compared to a 'real', unmodified flow.

The near-wall patch model previously developed by Carney *et al.* (2020) can be considered the lowest order asymptotic description of small-scale, near-wall dynamics in which the mean pressure gradient, the momentum flux from the outer flow and the mean wall shear stress are all uniform in time and space on the scale of the computational domain. To account for the relatively rapid downstream development of mean quantities in adverse-pressure-gradient boundary layers (Kitsios *et al.* 2017), we develop in the present work a higher-order approximation that allows the mean wall shear stress to develop slowly in the streamwise direction. Similar to Spalart (1988), Guarini *et al.* (2000), Maeder, Adams & Kleiser (2001) and Topalian *et al.* (2017), asymptotic analysis is used to derive a set of 'homogenized' equations that describe the mean effect of streamwise development on the near-wall dynamics.

If such a higher order computational model can be shown to accurately reproduce the near-wall, small-scale features of adverse-pressure-gradient flows, or, more generally, for

flows that feature asymptotic growth of mean quantities in the near-wall region, it could be used to inform a pressure-gradient dependent wall model for LES (Piomelli & Balaras 2002; Bose & Park 2018). In this setting, the model is a pressure-gradient-dependent analogue to the experimentally determined 'universal signal' of Mathis *et al.* (2011). Additionally, the model could be used to study the interaction between small-scale near-wall turbulent dynamics and more complicated physical processes such as heat transfer, chemical reactions, turbophoresis or surface roughness.

The rest of the paper is organized as follows. Section 2 motivates the slow-growth near-wall patch (SG-NWP) model and contains the multiscale asymptotic analysis on which the model is based. Section 3 then details the computational model and the numerical method used to integrate the equations of motion. Section 4 provides a comparison between the statistics generated by the model and the corresponding quantities from DNS for the cases of both zero and mild adverse pressure gradients. It is followed by a discussion and conclusions in §§ 5 and 6, respectively.

1.1. *Mathematical notation and nomenclature*

In the following discussion, the velocity components in the streamwise (x), wall-normal (y) and spanwise (z) directions are denoted as u, v and w, respectively, and when using index notation, these directions are labelled 1, 2 and 3, respectively. The expected value is denoted with angle brackets (as in $\langle\cdot\rangle$), and upper case U and P indicate the mean velocity and pressure, so that $\langle u_i\rangle = U_i$. The velocity and pressure fluctuations are indicated with primes, e.g. $u_i = U_i + u_i'$. Partial derivatives shortened to ∂_i signify $\partial/\partial x_i$, differentiation in the direction x_i. The mean advective derivative is $\mathrm{D}(\cdot)/\mathrm{D}t = \partial_t(\cdot) + U_j\partial_j(\cdot)$, where Einstein summation notation is implied. In general, repeated indices imply summation, with the exception of repeated Greek indices. Lastly, the superscript '$+$' denotes non-dimensionalization with the kinematic viscosity ν and the friction velocity u_τ.

2. Motivation

2.1. *Fundamental modelling assumptions*

Intrinsic to the computational model is the assumption of a separation of temporal and spatial scales between the small-scale turbulence arising from the autonomous near-wall dynamics and the large-scale outer-layer turbulence; this separation of scales occurs when the friction Reynolds number of the flow is asymptotically large. The near-wall dynamics are thus considered to be in local equilibrium with both the pressure gradient and momentum flux environment in which they evolve, as explored by Zhang & Chernyshenko (2016) and Chernyshenko (2021). In the previous near-wall patch formulation of Carney *et al.* (2020), it was further assumed these quantities were uniform in space and time on the scale of the dynamics being simulated. In the current work, the assumption of a constant pressure gradient is retained, however, the local mean wall shear stress is allowed to vary slowly in the streamwise direction, which should allow for a higher order asymptotic description of near-wall turbulence than before. In particular, it is assumed that the rate of change of the viscous length scale is asymptotically small. Under these assumptions, the near-wall model will be representative of a variety of flows that are not in equilibrium overall, including those with non-constant pressure gradients. However, the modelling approach breaks down, for example, for a boundary layer near separation; see § 5 for some remarks on this case.

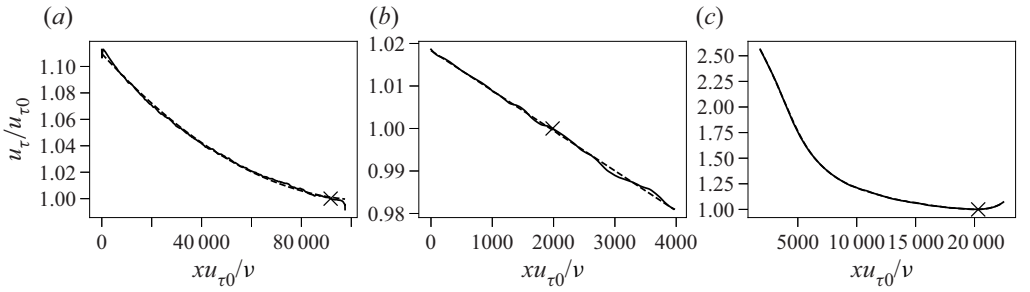

Figure 1. Friction velocity $u_\tau/u_{\tau 0}$ versus streamwise location $xu_{\tau 0}/\nu$ for each case in table 1, where $u_{\tau 0}$ is the value of the friction velocity at the locations marked '$\times$'. The dashed lines in panels (*a*) and (*b*) show quadratic and linear least-squares approximations, respectively, while that in panel (*c*) shows a piecewise cubic least-squares fit. (*a*) SJM-β0, (*b*) KS-β1 and (*c*) BVOS-β1.7.

2.2. *Growth effects in the near-wall region of turbulent boundary layers*

Consider a flat plate turbulent boundary layer that is homogeneous in the spanwise direction and under the influence of a pressure gradient in the streamwise direction. Let the pressure gradient be parameterized by

$$\beta = \frac{\delta^*}{\tau_w}\frac{\mathrm{d}P_\infty}{\mathrm{d}x}, \tag{2.1}$$

which is the standard non-dimensional Clauser parameter, where δ^* is the boundary layer displacement thickness, τ_w is the mean shear stress at the wall and $\mathrm{d}P_\infty/\mathrm{d}x$ is the far-field pressure gradient with a unit density. For any $\beta \in [0, \infty)$, the boundary layer as a whole will grow in the streamwise direction; *a fortiori*, so too will the near-wall region. Below we make two observations about the effect this growth has on the near-wall region of turbulent boundary layers (TBLs). These observations motivate the multiscale asymptotic analysis that will inform the slow-growth near-wall patch model.

The first observation is that the near-wall region of TBLs grows more rapidly with increasing β. As τ_w evolves downstream, so too does the viscous length scale characterizing the local near-wall scaling. Figure 1 illustrates the streamwise evolution of the friction velocity u_τ for the three large-scale simulation cases considered throughout this work, namely SJM-β0 (Sillero, Jiménez & Moser 2013), KS-β1 (Kitsios *et al.* 2017) and BVOS-β1.7 (Bobke *et al.* 2017), labelled by the value of the Clauser parameter (2.1) at the streamwise locations marked in each case by '$\times$' in the figure. Each friction velocity and streamwise location is scaled by the kinematic viscosity and value of u_τ at these particular locations, denoted below by $\bar{x}$.

As described in § 3, the model statistics are a function of the wall-normal direction only; that is, statistics are homogeneous in the stream and spanwise directions. In contrast, statistics of the TBLs to which the model is compared are only homogeneous in the spanwise direction. Hence, comparisons can only be made at particular streamwise locations $\bar{x}$. For SJM-β0, $\bar{x}$ is selected as the location with the largest value of Re_τ for which statistical profiles are reported, while $\bar{x}$ is selected for the BVOS-β1.7 case to maximize Re_τ before boundary effects from the 'fringe region' used to periodically match the TBL inlet and outlet profiles (Bobke *et al.* 2017) affect the statistics (this fringe region corresponds to the locations in figure 1(*c*) where $\partial u_\tau/\partial x$ is positive). The reason for maximizing Re_τ is to make comparisons at locations where the modelling ansantz

Large scale simulation	Re_τ	β	$\mathrm{d}P^+/\mathrm{d}x^+$	ϵ
SJM2000	1989.4	0	0	-2.985×10^{-7}
KS-β1	184.6	1.02	5.503×10^{-3}	-9.4303×10^{-6}
BVOS-β1.7	760.1	1.72	8.981×10^{-3}	-1.064×10^{-5}

Table 1. Parameters from the large-scale simulations considered at the streamwise location marked '$\times$' in figure 1.

just described in § 2.1 is most valid. Since both β and Re_τ are approximately constant throughout the domain for the KS-β1 simulation, $\bar{x}$ is simply taken in the middle.

The rate of change of the friction velocity with respect to streamwise position x can be used to define a length scale L that quantifies the streamwise distance over which the near-wall region grows. Define L by

$$L^{-1} = \frac{1}{u_\tau}\frac{\partial u_\tau}{\partial x}, \tag{2.2}$$

where both u_τ and $\partial u_\tau/\partial x$ are evaluated at $\bar{x}$. Using also the viscous length scale l_ν at $\bar{x}$, define the non-dimensional asymptotic parameter

$$\epsilon = \frac{l_\nu}{L} = \frac{\nu}{u_\tau^2}\frac{\partial u_\tau}{\partial x}. \tag{2.3}$$

The value of ϵ for each TBL case shown in figure 1 ranges from approximately 10^{-5} to 10^{-7}, as listed in table 1. For SJM-β0 and KS-β1, the derivative $\partial u_\tau/\partial x$ is estimated by differentiating a quadratic and linear least-squares approximation to u_τ. The u_τ data are relatively noisy in the BVOS case, so the data are first filtered with a Savitzky–Golay filter (Savitzky & Golay 1964) and it is then separately fit to a piecewise cubic spline interpolant. The derivative $\partial u_\tau/\partial x$ is then taken to be the average of the derivatives of these two approximations.

The dimensionless parameter ϵ is readily seen to be the (negative) streamwise rate of change of the viscous length scale, and it can also be taken as the inverse Reynolds number based on L and u_τ,

$$Re_\epsilon = L/l_\nu. \tag{2.4}$$

The asymptotic analysis detailed in § 2.3 is then valid for asymptotically large Re_ϵ; the infinite Re_ϵ limit corresponds to zero-growth of the near-wall layer, e.g. in a channel or pipe flow, while the vanishing Re_ϵ limit corresponds to boundary layer separation.

The second observation about growth effects in the near-wall region of TBLs is that there is an increase in momentum flux towards the wall with increasing β; in particular, the Reynolds shear stress increases in magnitude. To quantify this, consider the mean stress balance in viscous units for a TBL with (locally) constant pressure gradient $\mathrm{d}P/\mathrm{d}x$:

$$1 + \frac{\mathrm{d}P^+}{\mathrm{d}x^+}y^+ = \frac{\partial U^+}{\partial y^+} - \langle u'v'\rangle^+ - \int_0^{y^+}\left(U^+\frac{\partial U^+}{\partial x^+} + V^+\frac{\partial U^+}{\partial s^+} + \frac{\partial}{\partial x^+}\langle u'u'\rangle^+ - \frac{\partial^2 U^+}{\partial x^+ \partial x^+}\right)\mathrm{d}s. \tag{2.5}$$

Note that here s is just a dummy variable of integration. As $\mathrm{d}P^+/\mathrm{d}x^+$ increases, so too must the mean total stress on the right-hand side of (2.5). Figure 2 illustrates this balance

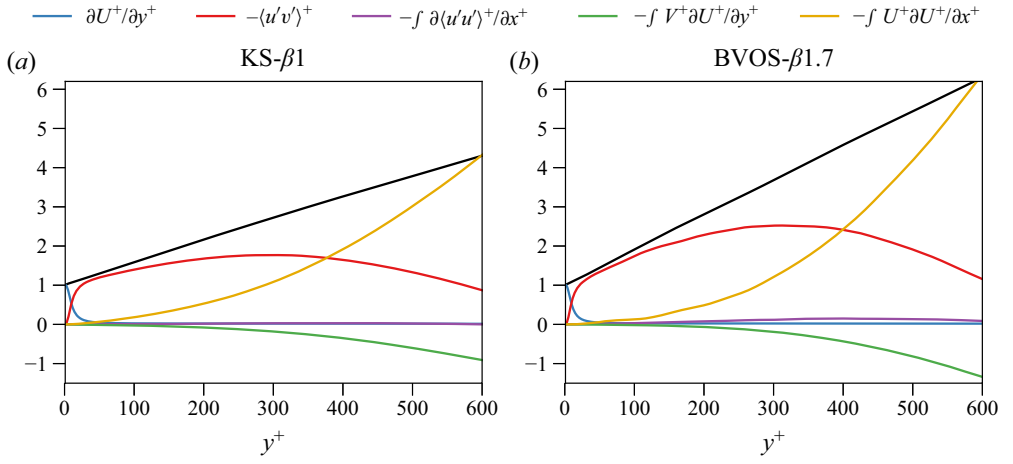

Figure 2. Contributions to the total stress (2.5) versus y^+ for the (*a*) KS-β1 case and (*b*) BVOS-β1.7 case. The black curves show the sum of all contributions, i.e. the right-hand side of (2.5).

for the two mild adverse-pressure-gradient TBL flows KS-β1 and BVOS-β1.7, where, as before, quantities are scaled in viscous units at the locations marked '$\times$' in figure 1. In addition to the Reynolds shear stress, the mean convective terms make a significant contribution to the stress balance, even in the near-wall region $y^+ \leq 300$. In contrast, the mean convective terms from SJM-β0 make a negligible contribution to the overall stress balance (not shown). In all cases, the mean viscous and turbulent fluctuation growth terms in (2.5) do not make a meaningful contribution to the total stress balance.

Large-scale numerical simulation of turbulent boundary layers properly account for the effect of boundary layer growth on the near-wall region simply by computing on domains that are sufficiently large. Clever 'recycling' and rescaling techniques (Lund, Wu & Squires 1998; Colonius 2004; Araya *et al.* 2011; Sillero *et al.* 2013) are typically used to increase size of the part of the domain containing 'healthy' turbulence (i.e. turbulence not impacted by inflow-outflow artefacts) while ensuring the simulations remain computationally affordable. Spalart (1988), however, took an alternative approach to achieve this goal. Assuming a scale separation between the size of the boundary layer and the streamwise length over which it develops, asymptotic analysis was used to determine a set of 'homogenized' equations of motion featuring the standard Navier–Stokes equations augmented with additional terms modelling the effect of boundary layer growth.

Inspired by the approach of Spalart (1988), we now describe a multiscale analysis to build a near-wall patch representation of the near-wall, small-scale dynamics of turbulent flows with asymptotically small ϵ. In this case, the separation of scales assumed in Spalart (1988) is expected to be even stronger, since only the near-wall layer is of interest, in contrast to the entire boundary layer.

2.3. *Multiscale asymptotic analysis*

The goal of the following analysis is to derive a set of equations for a near-wall patch domain that can produce accurate near-wall statistics for spatially developing flows.

First, if the viscous length scale evolves over distances that are asymptotically large relative to its local values, it is sensible to hypothesize a scaling relationship for the fluid

velocity of the form

$$u_i(x, y, z) = u_\tau(\epsilon x^+)u_i^+(x^+, y^+, z^+), \tag{2.6}$$

where ϵ is the dimensionless order parameter (2.3) and u_i^+ is considered statistically homogeneous in the stream and spanwise directions. This homogeneity will allow for the use of periodic boundary conditions (and Fourier spectral discretizations) for the near-wall patch domain, as done by Spalart (1988). The superscript '+' here denotes non-dimensionalization by the local viscous scale. Equation (2.6) is nothing but the standard near-wall viscous scaling where the friction velocity evolves slowly in the streamwise direction.

For some specific streamwise location $\bar{x}$, let

$$\overline{l_\nu} := l_\nu|_{x=\bar{x}} \tag{2.7}$$

denote the local viscous length scale, and let L be the length scale defined by (2.2); that is, the inverse of the logarithmic derivative of u_τ. For some given ϵ, define $X = \epsilon x$ as well as the new coordinates

$$(x, y, z) \mapsto (x/\overline{l_\nu}, yu_\tau(X^+)/\nu, z/\overline{l_\nu}) =: (x^+, \eta^+, z^+). \tag{2.8}$$

Note that in the definition of η^+, the argument in the friction velocity u_τ is $X^+ = \epsilon x/\overline{l_\nu} = x/L$.

The plan now is to first transform the incompressible Navier–Stokes equations from Cartesian to (x^+, η^+, z^+) coordinates and then insert the scaling hypothesis (2.6) into the result.

To transform the mass and momentum equations to the new coordinates (2.8), first note that derivatives transform as

$$\frac{\partial}{\partial x} \mapsto 1/\overline{l_\nu}\frac{\partial}{\partial x^+} + \epsilon/\overline{l_\nu}\eta^+\frac{\partial \log(u_\tau)}{\partial X^+}\frac{\partial}{\partial \eta^+}, \tag{2.9}$$

$$\frac{\partial}{\partial y} \mapsto 1/l_\nu(X^+)\frac{\partial}{\partial \eta^+}, \tag{2.10}$$

$$\frac{\partial}{\partial z} \mapsto 1/\overline{l_\nu}\frac{\partial}{\partial z^+}, \tag{2.11}$$

where $l_\nu(X^+) = \nu/u_\tau(X^+)$. Inserting the transformations in the continuity equation

$$\frac{\partial u_i}{\partial x_i} = 0 \tag{2.12}$$

gives

$$\frac{\partial u}{\partial x^+} + \overline{l_\nu}/l_\nu(X^+)\frac{\partial v}{\partial \eta^+} + \frac{\partial w}{\partial z^+} + \epsilon\eta^+\frac{\partial \log(u_\tau)}{\partial X^+}\frac{\partial u}{\partial \eta^+} = 0. \tag{2.13}$$

After additionally scaling by the viscous time scale at $\bar{x}$

$$\overline{t_\nu} := \left.\frac{\nu}{u_\tau^2}\right|_{x=\bar{x}}, \tag{2.14}$$

the streamwise component of the momentum equation transforms to

$$\begin{aligned}&\overline{l_\nu}/\overline{t_\nu}\frac{\partial u}{\partial t^+}+u\frac{\partial u}{\partial x^+}+\overline{l_\nu}/l_\nu(X^+)v\frac{\partial u}{\partial \eta^+}+w\frac{\partial u}{\partial z^+}+\epsilon\eta^+\frac{\partial\log(u_\tau)}{\partial X^+}u\frac{\partial u}{\partial \eta^+}\\&\quad+\frac{\partial p}{\partial x^+}+\epsilon\eta^+\frac{\partial\log(u_\tau)}{\partial X^+}\frac{\partial p}{\partial \eta^+}-\nu/\overline{l_\nu}\frac{\partial^2 u}{\partial x^+\partial x^+}-\nu/\overline{l_\nu}\frac{\partial^2 u}{\partial z^+\partial z^+}\\&\quad-\nu\overline{l_\nu}/l_\nu^2(X^+)\frac{\partial^2 u}{\partial \eta^+\partial \eta^+}-2\epsilon\nu\eta^+/l_\nu(X^+)\frac{\partial\log(u_\tau)}{\partial X^+}\frac{\partial^2 u}{\partial x^+\partial \eta^+}=0,\end{aligned}\tag{2.15}$$

where the $O(\epsilon^2)$ terms have been dropped. Similar terms appear for the other components. So far, the equations have simply been recast into new coordinates. In (2.15), the advective derivative is on the first line while the pressure gradient is on the second; the viscous terms are on both the second and third.

The next step is to hypothesize that the velocity and pressure fields scale with $u_\tau(X^+)$ and $u_\tau^2(X^+)$, respectively, as in (2.6). Using the superscript '+' to denote this scaling, the continuity equation (2.13) becomes

$$\frac{\partial u^+}{\partial x^+}+\overline{l_\nu}/l_\nu(X^+)\frac{\partial v^+}{\partial \eta^+}+\frac{\partial w^+}{\partial z^+}+\epsilon\frac{\partial\log(u_\tau)}{\partial X^+}\frac{\partial}{\partial \eta^+}(\eta^+u^+)=0.\tag{2.16}$$

Recall that the multiscale assumption underlying this analysis asserts that, at any given streamwise location, the ϵ-dependent slow-growth terms evolve over asymptotically large distances relative to the local viscous length scale; in particular then at $x=\bar{x}$, (2.16) simplifies to

$$\left(\frac{\partial u^+}{\partial x^+}+\frac{\partial v^+}{\partial y^+}+\frac{\partial w^+}{\partial z^+}\right)+\epsilon\frac{\partial}{\partial y^+}(y^+u^+)=0,\tag{2.17}$$

since at $x=\bar{x}$,

$$\frac{\partial\log(u_\tau)}{\partial X^+}=\frac{\overline{l_\nu}}{\epsilon}\frac{\partial\log(u_\tau)}{\partial x}(\bar{x})=1\tag{2.18}$$

and $l_\nu(X^+)=\overline{l_\nu}$. Note that in (2.17), y^+ denotes η^+ at $\bar{x}$. The same procedure of inserting the scaling assumptions and insisting they hold at $x=\bar{x}$ results in

$$\begin{aligned}&\frac{\partial u_i^+}{\partial t^+}+u^+\frac{\partial u_i^+}{\partial x^+}+v^+\frac{\partial u_i^+}{\partial y^+}+w^+\frac{\partial u_i^+}{\partial z^+}+\epsilon u^+\frac{\partial}{\partial y^+}(y^+u_i^+)\\&\quad+\left(\frac{\partial p^+}{\partial x^+}+\epsilon\left(y^+\frac{\partial p^+}{\partial y^+}+2p^+\right)\right)\delta_{1i}+\frac{\partial p^+}{\partial y^+}\delta_{2i}+\frac{\partial p^+}{\partial z^+}\delta_{3i}\\&\quad-\left(\frac{\partial^2}{(\partial x^+)^2}+\frac{\partial^2}{(\partial y^+)^2}+\frac{\partial^2}{(\partial z^+)^2}\right)u_i^+-2\epsilon\frac{\partial^2}{\partial x^+\partial y^+}(y^+u_i^+)=0\end{aligned}\tag{2.19}$$

for the ith component of the momentum equation; again the $O(\epsilon^2)$ have been neglected.

Equation (2.19) contains $O(\epsilon)$ terms originating from convective, pressure and viscous effects. Recall, however, that the contribution to the mean stress balance from the viscous streamwise growth term (the final term in the integral in (2.5)) is negligible in the adverse-pressure-gradient flows discussed in § 2.2. Hence, the $O(\epsilon)$ viscous terms are dropped, as was done in Spalart (1988). Similarly, the $O(\epsilon)$ pressure terms are dropped, since the pressure gradient is assumed to be constant over the length scales of the near-wall patch domain (as mentioned in § 2.1). Thus, only the convective growth terms remain.

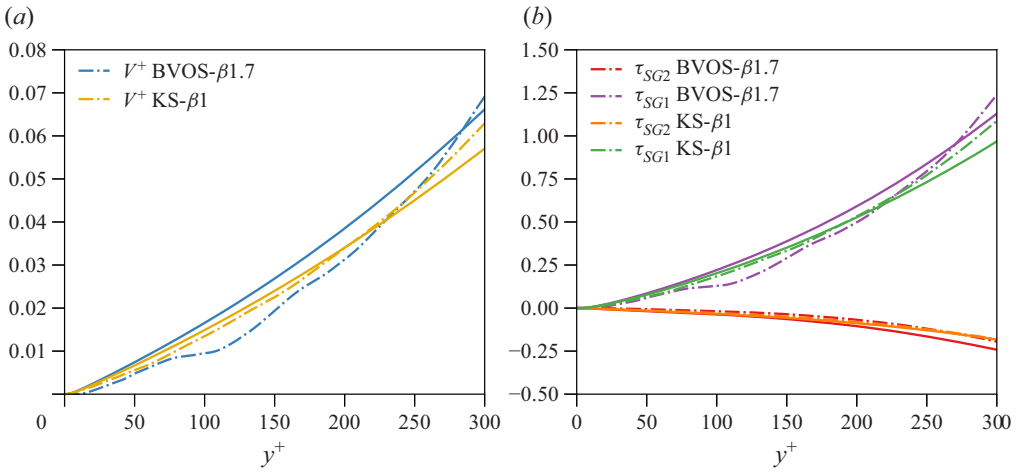

Figure 3. *A priori* slow-growth approximation of (*a*) the mean wall-normal velocity V^+ and (*b*) the stress terms (2.23) and (2.24) for KS-β1 and BVOS-β1.7. The approximations are shown as solid lines, while the quantities taken directly from the large-scale simulations are shown as dash–dotted lines.

Using index notation, the simplified momentum equation becomes

$$\frac{\partial u_i^+}{\partial t^+} + u_j^+ \frac{\partial u_i^+}{\partial x_j^+} + \frac{\partial p^+}{\partial x_i^+} - \frac{\partial^2 u_i^+}{\partial x_j^+ \partial x_j^+} + \epsilon u^+ \frac{\partial}{\partial y^+}(y^+ u_i^+) = 0. \tag{2.20}$$

For numerical purposes, it is useful to rewrite (2.20) in conservative form. Because of the slow-growth contribution to the continuity equation (2.17), however, an additional $O(\epsilon)$ convective term appears:

$$\frac{\partial u_i^+}{\partial t^+} + \frac{\partial}{\partial x_j^+}(u_i^+ u_j^+) + \frac{\partial p^+}{\partial x_i^+} - \frac{\partial^2 u_i^+}{\partial x_j^+ \partial x_j^+} + \epsilon \left(u^+ u_i^+ + \frac{\partial}{\partial y^+}(y^+ u^+ u_i^+) \right) = 0. \tag{2.21}$$

Note that this multiscale analysis was carried out starting with the incompressible Navier–Stokes equations in Cartesian coordinates written in convective form. If instead one starts with the equations written in conservative form, makes the same coordinate transformation (2.8) and scaling assuming (2.6), and retains only the $O(\epsilon)$ convective terms, then (2.21) will result.

2.4. *A priori test of SG model*

From the scaling assumption (2.6), the velocity components u_i^+ are homogeneous in the stream and spanwise directions. At statistical equilibrium, the slow-growth continuity equation (2.17) then implies that

$$V^+ = -\epsilon y^+ U^+. \tag{2.22}$$

Using data from the adverse-pressure-gradient simulations KS-β1 and BVOS-β1.7, one can use (2.22) as an *a priori* test of the slow-growth asymptotics just detailed. In general, the relationship (2.22) is expected to be relatively accurate close to the wall and at large Re_τ and large Re_ϵ, since it was derived under 'slowly developing' viscous scaling ansatz (2.6).

Figure 3(*a*) illustrates that the expression on the right-hand side of (2.22) matches the true wall-normal mean velocity V^+ up to a relative error of at most 8.6 % for the KS-β1 case. The accuracy is not as high in the BVOS-β1.7 case; however, the V^+ profile is relatively noisy in this case. Since the NWP model detailed below aims to simulate wall turbulence in the region $y^+ \in [0, 300]$, the profiles are shown in this range. In both cases, the discrepancy between the wall-normal mean velocity and its approximation increases for $y^+ \gtrsim 300$, since, at the relatively low values of Re_τ at which the large-scale simulations were conducted, wall scaling becomes inappropriate at relatively low values of y^+.

Slow-growth approximations can also be evaluated *a priori* for the mean convection terms which were shown in figure 2 to be important to the stress balance (2.5) of adverse-pressure-gradient turbulent boundary layers in the near-wall region. Equation (2.22) implies that, in viscous units, $-\int_0^y V\partial_y U \,\mathrm{d}s$ is approximated by

$$\tau^+_{SG1} := \int_0^{y^+} \epsilon s^+ U^+ \frac{\partial U^+}{\partial s^+} \,\mathrm{d}s^+, \tag{2.23}$$

while the coordinate change (2.8) and scaling assumption (2.6) imply that in viscous units, $\int_0^y U\partial_x U \,\mathrm{d}s$ is approximated by

$$\tau^+_{SG2} := \int_0^{y^+} \epsilon U^+ \frac{\partial}{\partial s^+}(s^+ U^+) \,\mathrm{d}s^+. \tag{2.24}$$

Figure 3(*b*) shows that (2.23) and (2.24) are indeed accurate *a priori* approximations of the mean convection terms in the stress balance for the near-wall region $y^+ \leq 300$. The relative errors are no larger than 9 %; the exception is approximation (2.23) for the BVOS-β1.7 case. It inherits the noise from the V^+ profile and hence is not as accurate.

3. Model formulation

3.1. *Mathematical formulation*

The goal of the computational model is to simulate the small-scale turbulent dynamics in the near-wall region as a function of an imposed gradient only in a small, rectangular domain $\Omega = [0, L_x] \times [0, L_y] \times [0, L_z]$ localized to the boundary. In addition to the physical wall at $y = 0$ where the no-slip condition is applied, the other computational boundaries are non-physical and located where, in a large-scale simulation, there is a region of chaotic nonlinear dynamics. At the sidewalls, periodic boundary conditions are used. This is consistent with the main scaling assumption (2.6) underlying the multiscale analysis in § 2.3, since the velocity fields evolved in time are assumed to be statistically homogeneous in the stream and spanwise directions. Any statistical inhomogeneities are modelled by $O(\epsilon)$ slow-growth terms. At the upper computational boundary $y = L_y$, homogeneous Neumann and Dirichlet conditions are prescribed for the stream/spanwise and wall-normal velocities, respectively. Since these conditions do not allow for any momentum flux through the computational boundary, the model includes a 'fringe region' $y \in [L_y/2, L_y]$ in which the flow is forced to provide the momentum that is transported into the near-wall region (see figure 4 for an illustration). The forcing f is non-zero only in the fringe region and, given a constant pressure gradient $\mathrm{d}P/\mathrm{d}x$, it injects momentum in such a way that ensures that the model's wall shear stress at statistical equilibrium is unity, as in Carney *et al.* (2020). Because of the $O(\epsilon)$ slow-growth contributions to the momentum equation derived in § 2.3, f is time-dependent; the precise details are given after introducing the model equations of motion below.

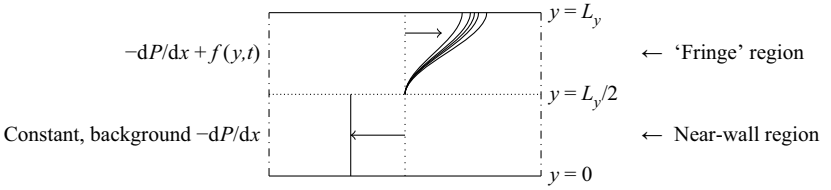

Figure 4. The fluid is subject to periodic boundary conditions at the dash–dotted side walls, homogeneous Dirichlet/Neumann conditions at the upper boundary $y = L_y$ and the no-slip condition at the wall $y = 0$. In addition to the constant pressure gradient assumed to be present in the near-wall layer, the model includes a time-dependent, auxiliary forcing function f (depicted here at multiple realizations in time) in a 'fringe region' $L_y/2 \le y \le L_y$ to make up for the momentum not transported at the computational boundary $y = L_y$.

The model equations of motion posed on the domain Ω are based on the slow-growth continuity (2.17) and momentum equations, and (2.21) from the asymptotic analysis of § 2.3, and they are discretized in the statistically homogeneous stream and spanwise directions with a Fourier–Galerkin method; however, there are a few differences in the equations that govern the horizontal averages

$$\bar{u}_i(y,t) = \frac{1}{L_x}\frac{1}{L_z}\int_0^{L_z}\int_0^{L_x} u_i(x,y,z,t)\,\mathrm{d}x\,\mathrm{d}z \tag{3.1}$$

and the fluctuations $u_i' = u_i - \bar{u}_i$.

First, the $(k_x, k_z) = (0,0)$ Fourier mode of the streamwise velocity ($\bar{u}$) evolves according to

$$\frac{\partial \bar{u}}{\partial t} + \frac{\partial}{\partial y}\overline{uv} + \epsilon_L\left(\overline{uu} + \frac{\partial}{\partial y}(y\overline{uu})\right) - \nu\frac{\partial^2 \bar{u}}{\partial y^2} = f - \frac{\mathrm{d}P}{\mathrm{d}x}, \tag{3.2}$$

which is simply the horizontal average of (2.21) (for $i = 1$) with additional forcing terms. Here, f is the fringe-region forcing whose explicit form is detailed below, while $\mathrm{d}P/\mathrm{d}x$ is the constant pressure gradient driving the flow in the near-wall region. Equation (3.2) is augmented with the no-slip condition at $y = 0$ and the homogeneous Neumann condition $\partial_y \bar{u} = 0$ at $y = L_y$. Note the parameter ϵ_L here necessarily has units of $1/\mathit{length}$, which is emphasized with the subscript 'L'. After detailing the forcing f, ϵ_L will be related back to the non-dimensional parameter (2.3).

Taking the horizontal average of the slow-growth continuity equation (2.17) gives

$$\frac{\partial \bar{v}}{\partial y} + \epsilon_L\frac{\partial}{\partial y}(y\bar{u}) = 0, \tag{3.3}$$

and the no-slip condition implies that $\bar{v} = -\epsilon_L y\bar{u}$, which is of course the analogue of the relation (2.22).

In contrast to $\bar{u}$, the evolution equation for the mean spanwise velocity $\bar{w}$ is not given by the horizontal average of (2.21) for $i = 3$. Instead, the $O(\epsilon)$ contributions involving $\bar{w}$ are neglected, as in Spalart (1988). Using

$$\overline{u'w'} = \overline{uw} - \bar{u}\bar{w}, \tag{3.4}$$

$\bar{w}$ evolves as

$$\frac{\partial \bar{w}}{\partial t} + \frac{\partial}{\partial y}\overline{vw} + \epsilon_L\left(\overline{u'w'} + \frac{\partial}{\partial y}(y\overline{u'w'})\right) - \nu\frac{\partial^2 \bar{w}}{\partial y^2} = 0, \tag{3.5}$$

with the no-slip condition and a homogeneous Neumann condition at $y = 0$ and $y = L_y$, respectively. This can be justified by the fact that the mean spanwise velocity $W = 0$ in

each of the large-scale simulations listed in table 1; it does not grow. Moreover, numerical stability issues can arise if one includes the $O(\epsilon)$ contributions involving $\bar{w}$, since the laminar equation for $\bar{w}$,

$$\frac{\partial \bar{w}}{\partial t} - \nu \frac{\partial^2 \bar{w}}{\partial y^2} = -\epsilon_L \bar{u}\bar{w}, \tag{3.6}$$

can exhibit exponential growth. Indeed, if $\epsilon_L < 0$ (as is the case for each large-scale simulation in table 1) and $\bar{u}$ is frozen in time, then $\bar{w} \sim \exp(-\epsilon_L \bar{u} t)$.

The Fourier modes $(k_x, k_z) \neq (0, 0)$ evolve as

$$\frac{\partial u_i}{\partial t} + \frac{\partial}{\partial x_j}(u_i u_j) + \epsilon_L \left(u u_i + \frac{\partial}{\partial y}(y u u_i) \right) + \frac{\partial p}{\partial x_i} - \nu \frac{\partial^2 u_i}{\partial x_j \partial x_j} = 0, \tag{3.7}$$

$$\frac{\partial u_i}{\partial x_i} = 0, \tag{3.8}$$

in which the $O(\epsilon)$ contribution to continuity is neglected, as in Spalart (1988). This appears to be a sensible approximation for boundary layers with mild β values; recall from figure 2 that the streamwise evolution of the turbulent kinetic energy made a negligible contribution to the mean stress balances of the KS-β1 and BVOS-β1.7 flows in the near-wall region. The slow-growth momentum equation (3.7) is augmented with the no-slip condition $u_i = 0$ at $y = 0$ and the no-flux conditions

$$v = 0, \quad \frac{\partial u}{\partial y} = \frac{\partial w}{\partial y} = 0 \text{ at } y = L_y. \tag{3.9}$$

The model equations are solved numerically using the velocity-vorticity formulation of Kim, Moin & Moser (1987), which is derived from (3.7) and (3.8) in the usual way (Lee 2015).

With all the equations of motion determined, the details of the forcing function f in the mean streamwise evolution equation (3.2) can now be specified. Its role is to provide momentum that will be transported to the near-wall region, and it is non-zero only in the fringe region $y > L_y/2$. It is constructed in such a way that, for a given set of values $\mathrm{d}P/\mathrm{d}x$ and ϵ_L, the model's equilibrium wall shear stress equals unity.

More specifically, from (3.2), the model's mean streamwise stress balance is

$$\tau_w + \frac{\mathrm{d}P}{\mathrm{d}x} y = \tau_{model}(y) + \int_0^y f \,\mathrm{d}s, \tag{3.10}$$

where, from the relation $V = -\epsilon_L y U$ (which follows from (3.3)), the model stress τ_{model} is

$$\tau_{model}(y) = \nu \frac{\partial U}{\partial y} - \langle u'v' \rangle - \epsilon_L \left(\int_0^y [U^2 + \langle u'u' \rangle] \,\mathrm{d}s + y \langle u'u' \rangle \right). \tag{3.11}$$

The no-flux boundary conditions imply that at $y = L_y$, (3.10) becomes

$$\int_0^{L_y} f \,\mathrm{d}y = \tau_w + \frac{\mathrm{d}P}{\mathrm{d}x} L_y + \epsilon_L \left(\int_0^{L_y} [U^2 + \langle u'u' \rangle] \,\mathrm{d}y + L_y \langle u'u' \rangle|_{y=L_y} \right). \tag{3.12}$$

If one then constrains f to satisfy

$$\int_0^{L_y} f \,\mathrm{d}y = 1 + \frac{\mathrm{d}P}{\mathrm{d}x} L_y + \epsilon_L \left(\int_0^{L_y} [U^2 + \langle u'u' \rangle] \,\mathrm{d}s + L_y \langle u'u' \rangle|_{y=L_y} \right), \tag{3.13}$$

Model case	dP^+/dx^+	ϵ
NWP-ZPG	0	0
NWP-β1	5.503×10^{-3}	0
NWP-β1.7	8.981×10^{-3}	0
SG-NWP-ZPG	0	-2.985×10^{-7}
SG-NWP-β1	5.503×10^{-3}	-9.430×10^{-6}
SG-NWP-β1.7	8.981×10^{-3}	-1.064×0^{-5}

Table 2. Imposed pressure gradient and slow-growth parameters for the model cases presented. Each value was chosen to match the corresponding one from the large-scale simulations listed in table 1.

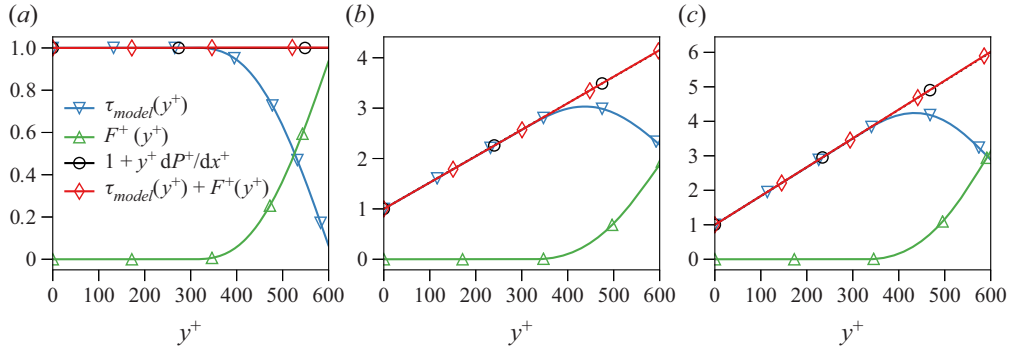

Figure 5. For each case in table 1, the model stress $\tau^+_{model}(y^+)$ (equation (3.11)) agrees with the target stress profile $\tau^+_{target}(y^+) = 1 + y^+ dP^+/dx^+$ for $y^+ \in [0, 300]$, while in the fringe region $y^+ \in [300, 600]$, the primitive $F^+(y^+)$ of the forcing function f supplies momentum flux so that $\tau^+_{model}(y^+) + F^+(y^+)$ agrees with the target stress throughout the entire domain $y^+ \in [0, 600]$. (*a*) SG-NWP-ZPG, (*b*) SG-NWP-β1 and (*c*) SG-NWP-β1.7.

the desired result $\tau_w = 1$ will follow. Assuming ergodicity, the identity

$$\langle A \rangle = \langle \bar{A} \rangle \tag{3.14}$$

is true for any field A. Hence, if at each point in time

$$\int_0^{L_y} f(y, t)\, dy = 1 + \frac{dP}{dx} L_y + \epsilon_L \left(\int_0^{L_y} \overline{uu}(y, t)\, dy + L_y \overline{u'u'}(L_y, t) \right) \tag{3.15}$$

holds, then (3.13) will result at equilibrium. The functional form of f is described in § 3.3. If one additionally sets the kinematic viscosity $\nu = 1$, then at equilibrium the model is scaled in viscous units, and the parameter ϵ_L reduces to the non-dimensional ϵ introduced in (2.3).

3.2. *Physical parameters*

Each slow-growth near-wall patch model case is parameterized by two inputs; they are the constant mean pressure gradient scaled in wall units dP^+/dx^+ and the asymptotic growth parameter ϵ given by (2.3). The values for the various model cases presented – two adverse-pressure-gradient cases and one zero-pressure-gradient case – are shown in table 2. Note that for each pressure gradient value, there is a model case both with ($\epsilon \neq 0$) and without ($\epsilon = 0$) growth effects included. Figure 5 illustrates the statistically converged

$L_x^+ = L_z^+$	L_y^+	N_x	N_z	N_y	Δx^+	Δz^+	Δy_w^+
1500	600	120	256	192	12.5	5.86	0.002817

Table 3. Summary of simulation parameters consistent for all simulation cases; N_x and N_z refer to the number of Fourier modes, while N_y is the number of B-spline collocation points. Here, $\Delta x = L_x/N_x$ and similarly for Δz, and Δy_w is the collocation point spacing at the wall.

stress balances for the three slow-growth model cases. As the imposed pressure gradient $\mathrm{d}P^+/\mathrm{d}x^+$ increases, the total momentum transport in the near-wall region increases, as noted in § 2.2.

3.3. *Computational parameters and numerical implementation*

The remaining model parameters, consistent for all simulation cases, are summarized in table 3 and are identical to those used by Carney *et al.* (2020). In particular, the size of the rectangular domain Ω is taken to be $L_x^+ = L_z^+ = 1500$ and $L_y^+ = 600$, selected based on the spectral analysis of Lee & Moser (2019). Their work suggests that, at least for the mild favourable-pressure-gradient cases considered, the contributions to the turbulent kinetic energy from modes with wavelengths $\lambda^+ < 1000$ are universal and Re_τ independent in the region $y^+ \lesssim 300$. Accordingly, L_y^+ is taken to be $2 \times 300 = 600$ to allow for a sufficiently large fringe region to mollify the effect of the non-physical computational boundary at $y = L_y$ (see figure 4). The values $L_x^+ = L_z^+ = 1500$ were chosen because they were found to be the smallest domain sizes capable of reproducing the universal small-scale turbulent kinetic energies identified in the channel flow simulations of Lee & Moser (2019) (see § 3.3 of Carney *et al.* 2020). The majority of statistics reported in this work were from simulations with these stream and spanwise dimensions; however, a range of values larger than 1500 were also explored to assess the dependence of the model statistics on the choice of L_x and L_z. In general, the statistics generated from these simulations exhibit little to no variation as the domain sizes grow. The streamwise and spanwise velocity variances are two exceptions to this, however. As discussed more fully in § 4.2, these statistics are known to be influenced by low-wavenumber, large-scale structures present in direct numerical simulations. As the NWP domain sizes grow, more of these large-scale structures are included, and hence the stream/spanwise velocity variances continually change with increasing L_x and L_z. The results are documented in the Appendix.

For a given selection of model parameters $(\mathrm{d}P^+/\mathrm{d}x^+, \epsilon)$, the forcing function f responsible for providing momentum flux to the near-wall region is constrained at each time step to satisfy (3.15); otherwise, however, it is not uniquely specified. For the simulations reported here, f is taken to be $f(y,t) = \psi(t)g(y)$, where g is a piecewise cubic function

$$g(y) = \begin{cases} 4/L_y^4(L_y - 2y)^2(5L_y - 4y) & y \in [L_y/2, L_y] \\ 0 & y \in [0, L_y/2] \end{cases}, \tag{3.16}$$

which satisfies

$$\int_{L_y/2}^{L_y} g(y)\,\mathrm{d}y = 1, \tag{3.17}$$

and $g(L_y/2) = g'(L_y/2) = g'(L_y) = 0$, so that the transition in forcing from the near-wall region to the fringe region is smooth. In general, other function forms for g are of course

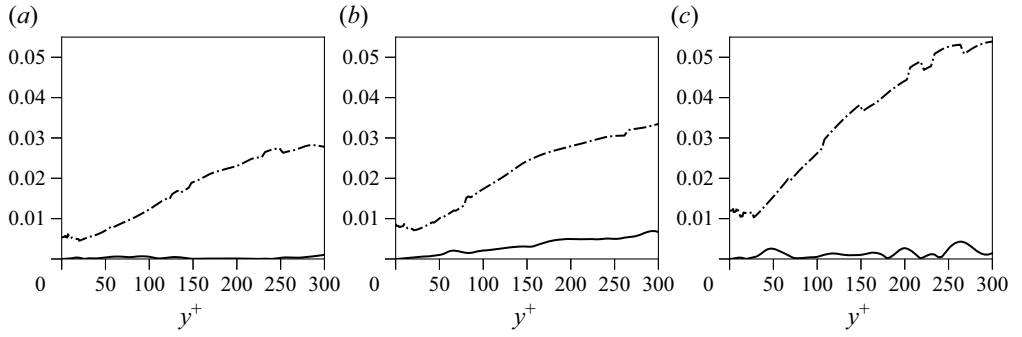

Figure 6. Statistical convergence for the slow-growth model cases listed in table 2: solid lines, absolute error $|\tau^+_{model}(y^+) - \tau^+_{target}(y^+)|$, where τ_{model} is defined in (3.11) and $\tau_{target} = \tau_w + y\,\mathrm{d}P/\mathrm{d}x$; dash–dotted lines, standard deviation of the estimated statistical error for τ^+_{model} in the region $y^+ \in [0, 300]$. (*a*) SG-NWP-ZPG, (*b*) SG-NWP-β1 and (*c*) SG-NWP-β1.7.

possible and, in particular, a quadratic profile satisfying (3.17) and $g(L_y/2) = g'(L_y/2) = 0$ was also implemented with no discernible changes in the statistics in the near-wall region $y^+ \in [0, 300]$. The time-dependent function ψ is defined as

$$\psi(t) = 1 + \frac{\mathrm{d}P}{\mathrm{d}x} L_y + \epsilon_L \left(\int_0^{L_y} \overline{uu}(y, t)\,\mathrm{d}y + L_y \overline{u'u'}(L_y, t) \right), \tag{3.18}$$

which is simply the right-hand side of the forcing constraint (3.15). Together, (3.17) and (3.18) ensure that the constraint (3.15) indeed holds.

As mentioned in § 3.1, the model is solved numerically using the velocity-vorticity formulation of Kim *et al.* (1987). The numerical method is identical to that employed by Carney *et al.* (2020) and Lee & Moser (2015), that is, a Fourier–Galerkin method and a seventh-order B-spline collocation method for the stream/spanwise directions and wall-normal direction, respectively. The equations of motion are integrated in time with a low-storage, third-order Runge–Kutta (RK) method that treats diffusive terms implicitly and convective terms explicitly (Spalart, Moser & Rogers 1991). Note that the forcing term $f(y, t)$ in the evolution equation (3.2) for $\bar{u}$ is a nonlinear (and non-local) expression, and it is thus treated explicitly in the RK scheme, like the other nonlinear terms.

The computational resolution in both time and space is chosen to be consistent with that of channel flow DNS. The number of Fourier modes (and corresponding effective resolutions) used in each model simulation are listed in table 3. They are comparable with, for example, the parameters listed in table 1 of Lee & Moser (2015). Additionally, the collocation point spacing in the wall-normal direction is similar to previous DNS studies; the total number of collocation points N_y below $y^+ = 600$, as well as their distribution Δy^+ in the near-wall region, are taken to be equal to the $Re_\tau = 1000$ case of Lee & Moser (2015). As done by Carney *et al.* (2020), the model is implemented in a modified version of the PoongBack DNS code (Lee, Malaya & Moser 2013; Lee *et al.* 2014).

3.4. *Statistical convergence*

The method of Oliver *et al.* (2014) is used to assess the uncertainty in the statistics reported due to sampling error. For each $(\mathrm{d}P^+/\mathrm{d}x^+, \epsilon)$ case listed in table 2, the statistics are collected by averaging in time until the estimated statistical uncertainty in the total model stress profile $\tau_{model}(y)$ (see (3.11)) is less than a few per cent. Figure 6 shows that the

sampling error $|\tau^+_{model}(y^+) - \tau^+_{target}(y^+)|$ (where $\tau_{target}(y) = \tau_w + y\,\mathrm{d}P/\mathrm{d}x$) is no larger than three per cent for each SG model case and, in particular, the errors are smaller than the uncertainties; the errors are similarly small for the $\epsilon = 0$ cases (not displayed).

4. Numerical results

Based on the underlying scale separation assumptions, the SG-NWP model can be interpreted in one of two complementary ways. In the first, one considers it to be a model for the small-scale near-wall turbulence in a wall-bounded flow with: (i) mean pressure gradient in wall units $\mathrm{d}P^+/\mathrm{d}x^+$ and (ii) rate of change of the viscous length scale ϵ identical to those imposed in the model. In this case, one aspires to have the statistics from the model agree with those of the real flow at some fixed streamwise location. Ideally, this match is exact for quantities that are insensitive to the unrepresented large-scale motions, while for others, the match holds after applying a high-pass filter, for example, for the streamwise velocity variance, as done by Lee & Moser (2019). This is the interpretation explored in the results reported here. In the second interpretation, the SG-NWP model represents the small-scale near-wall turbulence in a region of real wall-bounded turbulent flow with local (i.e. scaled with the local wall shear stress) values of $\mathrm{d}P^+/\mathrm{d}x^+$ and ϵ the same as those imposed in the model. In this case, the SG-NWP model is analogous to the universal signal of Mathis *et al.* (2011), representing the process that is modulated by large-scale outer-layer fluctuations in a real turbulent flow, and it is compatible with the quasi-steady, quasi-homogeneous description of the scale interactions in near-wall turbulence (Zhang & Chernyshenko 2016; Chernyshenko 2021). It is this second interpretation where one could potentially employ the model to inform a pressure-gradient-dependent wall-model for an LES, for example.

The statistics reported here were computed from SG-NWP model cases with three different pressure gradient values; for each value, a separate simulation with $\epsilon = 0$ was also conducted to help understand the impact of asymptotic slow-growth effects. The model statistics are compared with the three large-scale simulation cases described at the beginning of § 2.2: the zero-pressure-gradient case SJM-β0, as well as the adverse-pressure-gradient cases KS-β1 and BVOS-β1.7. The corresponding model cases are thus referred to as SG-NWP-ZPG, SG-NWP-β1 and SG-NWP-β1.7 ($\epsilon \neq 0$), and NWP-ZPG, NWP-β1 and NWP-β1.7 ($\epsilon = 0$). The pressure gradients imposed in the model correspond to the local values scaled in viscous units of the large-scale simulations at the streamwise location marked '$\times$' in figure 1, and the model's wall-normal statistical profiles are compared with those of the large-scale simulations at these streamwise locations. All model cases are summarized in table 2.

4.1. *Mean velocity and shear stresses*

Because the Reynolds stress of a zero-pressure-gradient boundary layer is dominated by small-scale near-wall turbulent fluctuations and growth effects are relatively insignificant, the mean velocity and Reynolds shear stress profiles from the NWP-ZPG model case are in excellent agreement with the corresponding DNS profiles (Carney *et al.* 2020). The $O(\epsilon)$ terms included in the SG-NWP-ZPG case only enhance the agreement; in particular, there is a modest improvement in the Reynolds stress profile for $y^+ \in [100, 300]$ from the NWP-ZPG case that reduces the maximum relative error from 4 % to 1.3 %, as shown in figure 7(*c*). The slow-growth terms seem to not have an effect on the mean velocity U^+, as the NWP-ZPG and SG-NWP-ZPG profiles are nearly identical. In both cases, the relative

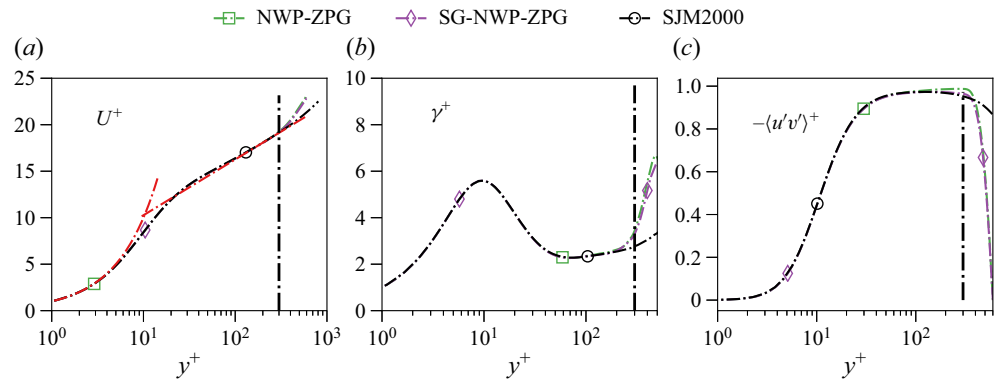

Figure 7. (*a*) Mean velocity U^+, (*b*) indicator function $\gamma^+ = y^+ \partial U^+/\partial y^+$ and (*c*) Reynolds stress $\langle u'v'\rangle^+$ versus y^+ for the zero-pressure-gradient simulation cases. The vertical, black dash–dotted lines mark the beginning of the fringe region $y^+ = 300$, and the law-of-the-wall $U^+ = y^+$ and $U^+ = (1/\kappa)\log(y^+) + B$ is also marked with a red dash–dotted line in panel (*a*), where $\kappa = 0.384$ and $B = 4.27$ (Lee & Moser 2015).

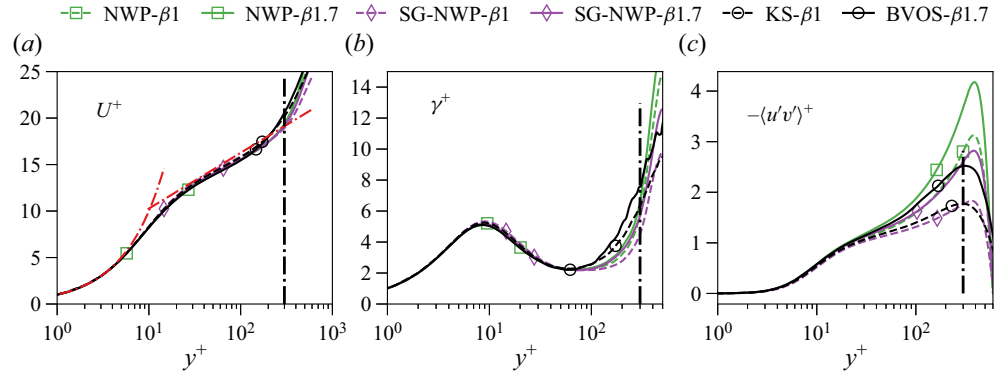

Figure 8. (*a*) Mean velocity U^+, (*b*) indicator function $\gamma^+ = y^+ \partial U^+/\partial y^+$ and (*c*) Reynolds stress $\langle u'v'\rangle^+$ versus y^+ for the adverse-pressure-gradient simulation cases. The vertical, black dash–dotted lines mark the beginning of the fringe region $y^+ = 300$, and the law-of-the-wall $U^+ = y^+$ and $U^+ = (1/\kappa)\log(y^+) + B$ is also marked with a red dash–dotted line in panel (*a*), where $\kappa = 0.384$ and $B = 4.27$ (Lee & Moser 2015).

error in U^+ is less than 0.6 % for $y^+ \in [0, 300]$, and the error is similarly small for the log-law indicator function γ^+,

$$\gamma^+(y^+) = y^+ \frac{\partial U^+}{\partial y^+}, \tag{4.1}$$

in the range $y^+ \in [0, 100]$. However, in both cases, there is mild disagreement of γ in the range $y^+ \in [100, 300]$. As expected, the profiles diverge for $y^+ > 300$; recall that $\langle u'v'\rangle$ necessarily vanishes as a consequence of the $v = 0$ condition posed (for Fourier modes $(k_x, k_z) \neq (0, 0)$) at the upper computational boundary $y = L_y$.

Since growth effects fundamentally alter the balance of momentum transport in the near-wall region for adverse-pressure-gradient boundary layers (recall figure 2), the model cases NWP-β1 and NWP-β1.7 that do not account for these effects are not expected to accurately reproduce the Reynolds shear stress profiles from the corresponding DNS and wall-resolved (WR)LES cases KS-β1 and BVOS-β1.7. Figure 8 indeed shows that this is the case; when $\epsilon = 0$, the model severely overestimates the target profiles for

$y^+ \in [70, 300]$. Including the $O(\epsilon)$ terms from the slow-growth analysis, however, leads to a significant improvement, as the SG-NWP-$\beta 1$ and SG-NWP-$\beta 1.7$ model cases both have a maximum error of approximately 9 % and 7 %, respectively, for $y^+ \in [0, 300]$. This remarkable improvement demonstrates that the SG-NWP model's $O(\epsilon)$ terms, as well as the forcing function f in the fringe-region $300 \leq y^+ \leq 600$, provide a good approximation of the momentum transport environment present in real, spatially developing wall-bounded turbulent flows with mild adverse pressure gradients.

Similar to the zero-pressure-gradient case, the mean velocity and log-law indicator profiles for the adverse-pressure-gradient model flows are essentially identical whether or not slow-growth effects are included. For all four adverse-pressure-gradient model cases, the relative error in the mean velocity profile U^+ is less than 6 % in the near-wall region $y^+ \in [0, 300]$. The error in the log-law indicator function γ^+ is similarly small for $y^+ \in [0, 80]$, while each model case underpredicts γ for $y^+ \in [80, 300]$. However, this underprediction appears to be slightly worse for the SG-NWP cases than for those with $\epsilon = 0$. From the mean stress balance (3.10), for $\epsilon = 0$, overprediction of the Reynolds shear stress implies underprediction of the mean viscous stress, however, the slow-growth terms present in (3.10) appear to be responsible for the underprediction when $\epsilon \neq 0$, given that the Reynolds stress is more accurate. As discussed in § 2.1, it is expected that the accuracy of the model would increase in the region $y^+ \in [80, 300]$ if it were compared with a DNS/WRLES flow at the same pressure gradient $\mathrm{d}P^+/\mathrm{d}x^+$ and growth parameter ϵ but larger Re_τ.

4.2. *Velocity variances*

For a wall-bounded flow in a full size domain, the low-wavenumber contributions to the Reynolds stress represent the mean influences of the large-scale structures on the near-wall dynamics. It is well established that for channel and zero-pressure-gradient boundary layer flows, these low-wavenumber features of the near-wall flow depend on Re_τ (Hutchins & Marusic 2007; Marusic *et al.* 2010*a*; Lee & Moser 2017; Samie *et al.* 2018; Lee & Moser 2019). Their contribution to the turbulent kinetic energy and their modulation of the small-scale, high-wavenumber energy both increase with increasing Re_τ. Experimental (Harun *et al.* 2013; Sanmiguel Vila *et al.* 2017, 2020) and computational (Lee 2017; Yoon *et al.* 2018; Tanarro *et al.* 2020; Pozuelo *et al.* 2022) studies have demonstrated that a similar result holds for adverse-pressure-gradient boundary layers; increasing the pressure gradient parameter β leads to a significant enhancement of the large-scale energy, both in the outer layer and in the near-wall region.

The SG-NWP model, by design, cannot accurately represent these large-scale structures, as it instead seeks to isolate the dynamics of the near-wall small-scales associated with the autonomous cycle of Jiménez & Pinelli (1999) from their influence. Since the stream and spanwise velocity variances in both the zero and adverse-pressure-gradient boundary layers considered here are known to depend on low-wavenumber contributions, the corresponding model profiles are not expected to be accurate. Figure 9 shows this is indeed the case. Although both the NWP-ZPG and SG-NWP-ZPG $\langle u'u' \rangle$ profiles appear to be in excellent agreement with the corresponding profile from Sillero *et al.* (2013), this is a serendipitous coincidence. For an experiment or simulation at a larger Re_τ, the streamwise velocity variance will grow (see figure 2 of Samie *et al.* (2018), for example), but it will be modelled by a similar SG-NWP flow; although ϵ may differ slightly, the pressure gradient will be the same. Similarly, at first glance, the model $\langle u'u' \rangle$ profiles in the adverse-pressure-gradient cases (figure 9*d–f*) are seen to be significantly larger than their large-scale simulation counterparts. However, it should be noted that the KS-$\beta 1$ and

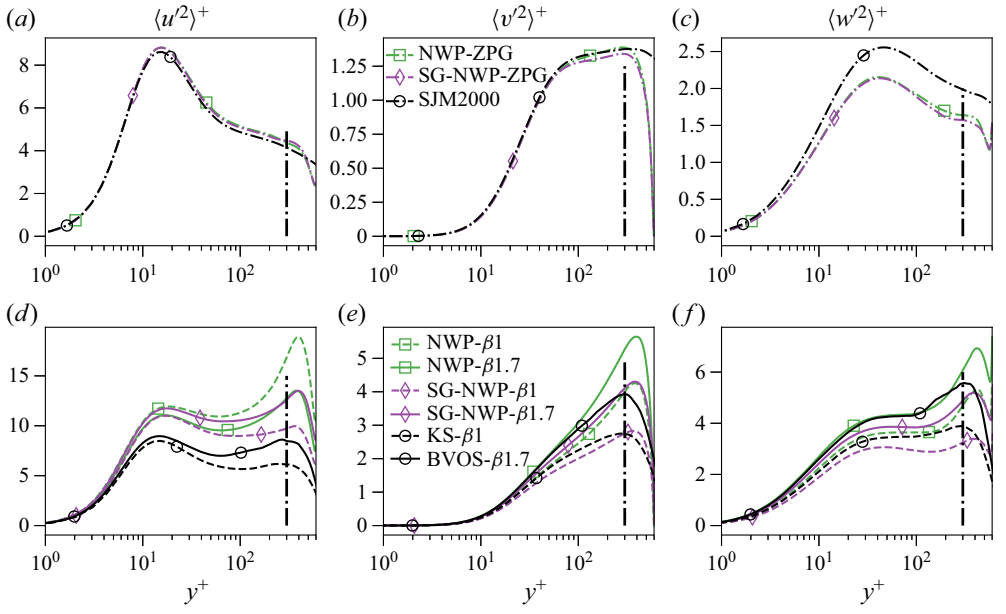

Figure 9. Velocity variances $\langle u'_\alpha u'_\alpha \rangle$ versus y^+ for (*a–c*) zero-pressure-gradient and (*d–f*) adverse-pressure-gradient simulations. The vertical, black dash–dotted lines mark the beginning of the fringe region $y^+ = 300$.

BVOS-β1.7 simulations are at relatively low Re_τ (see table 1); at fixed β values but larger Re_τ, the profiles would be larger (Sanmiguel Vila *et al.* 2020; Pozuelo *et al.* 2022).

In contrast to the stream and spanwise velocity variances, the impact of large-scale motions on the wall-normal velocity variance for zero and adverse-pressure-gradient boundary layers is less well documented. For channel flows, Lee & Moser (2019) established that the $\langle v'v' \rangle$ energy density in the near-wall region is concentrated primarily at wavelengths less than 1000 in viscous units, and hence the near-wall patch profiles from Carney *et al.* (2020) were indeed in agreement with those from large-scale simulations. Figure 9 suggests a similar result holds true for the near-wall region of adverse-pressure-gradient boundary layers. Although the agreement is not as good as the zero-pressure-gradient cases, the SG-NWP model $\langle v'v' \rangle$ profiles compare reasonably well with the KS-β1 and BVOS-β1.7 data; the maximum relative error for $y^+ \in [0, 300]$ is 14 % and 8.5 %, respectively. The NWP model without slow-growth effects, however, overpredicts the adverse-pressure-gradient wall-normal velocity variance, similar to the Reynolds shear stress profiles, illustrating the impact of the streamwise development of the mean wall shear stress τ_w on the near-wall turbulent kinetic energy.

4.3. *Small-scale turbulent kinetic energy*

Universal small-scale dynamics in the near-wall region associated with the autonomous cycle of Jiménez & Pinelli (1999) have been identified in channels (Lee & Moser 2019) and zero-pressure-gradient boundary layers (Samie *et al.* 2018) by applying a high-pass filter to the energy spectral density. Increases in the near-wall, small-scale energy have also been reported in adverse-pressure-gradient boundary layers due to amplitude modulation effects (Harun *et al.* 2013; Lee 2017; Yoon *et al.* 2018). Sanmiguel Vila *et al.* (2020) explicitly computed small-scale contributions to the near-wall turbulent kinetic energy. Using a

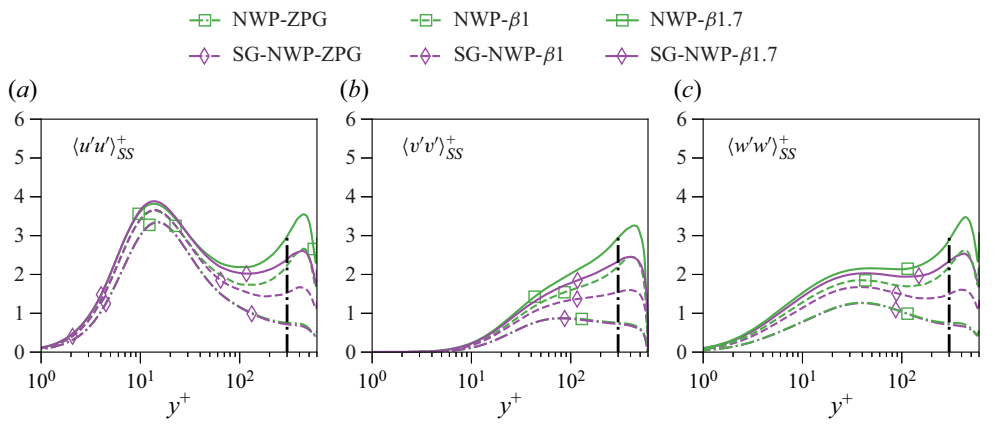

Figure 10. High-pass filtered velocity variances $\langle u'_\alpha u'_\alpha \rangle_{SS}$ versus y^+ for each model case listed in table 2. The vertical, black dash–dotted lines mark the beginning of the fringe region $y^+ = 300$.

cutoff wavelength of $\lambda_x^+ \approx 4300$, they found a collapse in the peak of the small-scale contribution to $\langle u'u' \rangle^+$ at $y^+ \approx 15$ for a range of β values from 0 to approximately 2.2. In contrast, Lee (2017) found that the small-scale contributions to the streamwise velocity variance increased with the pressure gradient, however, this result was based on a much more restrictive high-pass filter; all contributions from spanwise wavelengths $\lambda_z^+ \gtrsim 180$ were filtered out. Using the same filter as Carney *et al.* (2020) defined by (4.2) below, the small-scale near-wall energy from SG-NWP flows is found to increase with increasing pressure gradient, in agreement with the conclusion of Lee (2017).

Carney *et al.* (2020) directly compared the near-wall patch model's high-pass filtered Reynolds stress to the filtered profiles of several channel flow DNS of Lee & Moser (2019). After filtering out contributions from wavemodes that do not satisfy

$$\min\{|k_x|, |k_z|\} > k_{cut}, \tag{4.2}$$

where $k_{cut} = 2\pi/\lambda_{cut}$ and $\lambda_{cut}^+ = 1000$, the model's Reynolds stress profiles were in close agreement with the filtered DNS profiles, indicating the NWP model successfully reproduces the universal small-scale dynamics. Although the high-pass filtered Reynolds stresses of the present slow-growth NWP model cannot be directly compared with data from the literature, we report them here nonetheless to illustrate the effect of pressure gradient and growth on the small-scale energies.

Let $\mathcal{K}$ denote the set of all wavenumbers included in an SG-NWP simulation, and let $k = 2\pi/\lambda_{cut}$ with $\lambda_{cut}^+ = 1000$ as just mentioned. Define $\mathcal{K}_{SS}$ to be the subset of $\mathcal{K}$ with the property that $(k_x, k_z) \in \mathcal{K}_{SS}$ if (4.2) holds. If E_{ij} denotes the Fourier transform of the two point correlation tensor

$$R_{ij}(r_x, y, r_z) = \langle u'_i(x + r_x, y, z + r_z) u'_j(x, y, z) \rangle \tag{4.3}$$

in the variables r_x and r_z, then the small-scale energies shown in figure 10 are defined to be

$$\langle u'_i u'_j \rangle_{SS}(y) = \sum_{(k_x,k_z)\in\mathcal{K}_{SS}} E_{ij}(k_x, y, k_z). \tag{4.4}$$

It is clear that for each component $\langle u'_\alpha u'_\alpha \rangle$, the model's near-wall, small-scale energy increases as the pressure gradient $\mathrm{d}P^+/\mathrm{d}x^+$ increases, whether or not slow-growth

effects are included. The agreement between simulations with and without $O(\epsilon)$ terms is particularly strong for the streamwise small-scale energy in the region $y^+ \lesssim 50$, suggesting that the increase in small-scale, near-wall energy in this region can be attributed solely to the adverse-pressure-gradient effects, and not to growth effects.

4.4. *Turbulent kinetic energy budget*

The mean dynamics of the turbulent kinetic energy $k = u_i' u_i'/2$ are governed by the turbulent kinetic energy (TKE) budget equation

$$\frac{\mathrm{D}\langle k\rangle}{\mathrm{D}t} = \overbrace{-\langle u_i' u_j'\rangle \frac{\partial U_i}{\partial x_j}}^{\mathcal{P}_k} \overbrace{-\frac{\partial \langle k u_j'\rangle}{\partial x_j}}^{T_k} \overbrace{+\nu \frac{\partial^2 \langle k\rangle}{\partial x_j \partial x_j}}^{D_k} \overbrace{-\frac{\partial \langle p' u_j'\rangle}{\partial x_j}}^{\Upsilon_k} \overbrace{-\nu \left\langle \frac{\partial u_i'}{\partial x_j}\frac{\partial u_i'}{\partial x_j}\right\rangle}^{\varepsilon_k}. \tag{4.5}$$

For a wall-bounded turbulent flow that is homogeneous in the spanwise direction and slowly developing in the streamwise direction, one can derive a 'slow-growth' version of (4.5) using the same multiscale asymptotic analysis outlined in § 2.3; namely, one transforms x and y according to (2.8) and then inserts the scaling ansatz (2.6) into the resulting equation. The resulting 'slow-growth' TKE budget equation can be shown to be

$$\begin{aligned}
\overbrace{2\epsilon \langle k\rangle^+ U^+}^{\text{SG Adv.}} = &- \overbrace{\left(\langle u'v'\rangle^+ \frac{\partial U^+}{\partial y^+} + \epsilon \frac{\partial}{\partial y^+}(y^+ U^+)[\langle u'u'\rangle^+ - \langle v'v'\rangle^+] \right)}^{\mathcal{P}^+_{k,SG}} \\
&- \overbrace{\left(\frac{\partial}{\partial y^+}\langle kv'\rangle^+ + 3\epsilon \langle ku'\rangle^+ + \epsilon\, y^+ \frac{\partial}{\partial y^+}\langle ku'\rangle^+ \right)}^{T^+_{k,SG}} \\
&- \overbrace{\left(\frac{\partial}{\partial y^+}\langle p'v'\rangle^+ + 3\epsilon \langle p'u'\rangle^+ + \epsilon\, y^+ \frac{\partial}{\partial y^+}\langle p'u'\rangle^+ \right)}^{\Upsilon^+_{k,SG}} \\
&+ \overbrace{\frac{\partial^2}{(\partial y^+)^2}\langle k\rangle^+}^{D^+_{k,SG}} - \overbrace{\left\langle \frac{\partial u_i'}{\partial x_j}\frac{\partial u_i'}{\partial x_j}\right\rangle^+}^{\varepsilon^+_{k,SG}},
\end{aligned} \tag{4.6}$$

where the $O(\epsilon^2)$ contributions are neglected. If one alternatively starts with the slow-growth continuity (2.17) and momentum (2.19) equations from § 2.3 and derives an equation governing the dynamics of $\langle u_i' u_i'\rangle^+/2$ in the standard way, then, modulo $O(\epsilon^2)$ terms, nearly the same exact equation will result. The only difference is that, in this latter derivation, an extra $O(\epsilon)$ correction to the dissipation ε_k appears that is not present in (4.6). The term is proportional to $y\langle u_i' \partial_x \partial_y u_i'\rangle$ and arises from the $O(\epsilon)$ viscous term in (2.19).

Because the SG-NWP model momentum equation (3.7) neglects some of the $O(\epsilon)$ terms that arise from the asymptotic analysis in § 2.3, there are some discrepancies between (4.6) and the model's TKE budget equation. In particular, there are discrepancies in the production $\mathcal{P}_{k,SG}$, as well as the turbulent and pressure transport terms $T_{k,SG}$ and $\Upsilon_{k,SG}$. Although the errors introduced by these discrepancies are in each case relatively small, they are documented below when comparing the model's TKE budget to those of the large-scale simulations.

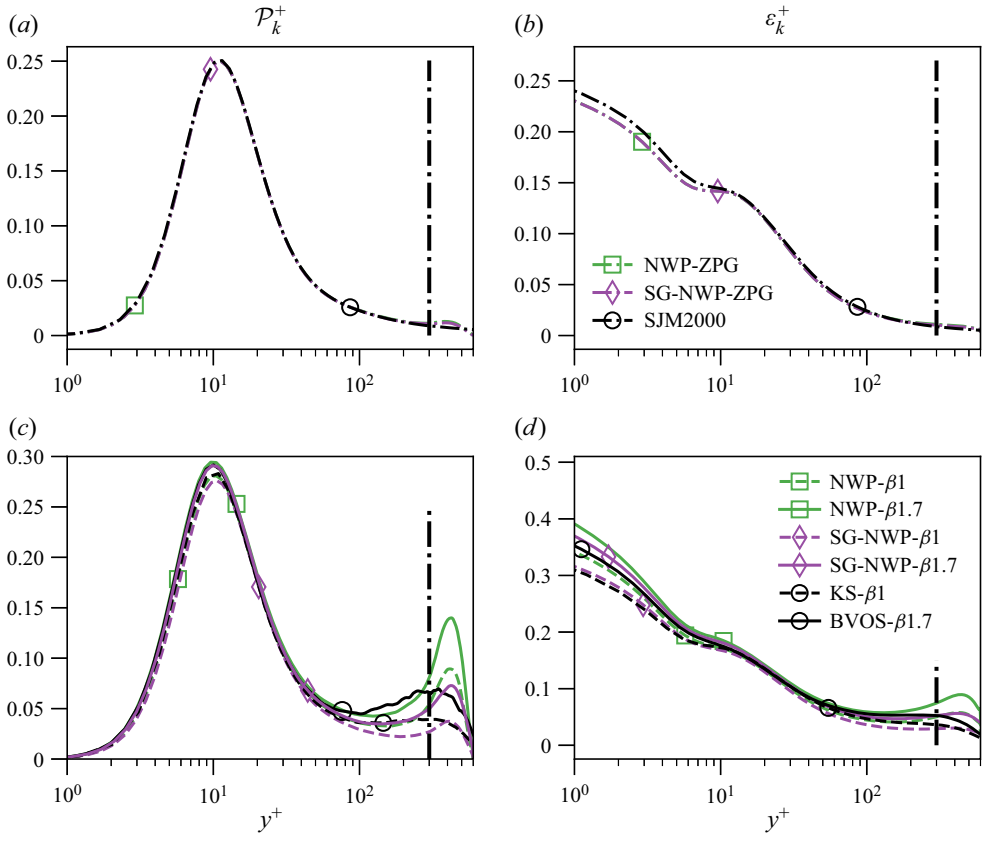

Figure 11. (*a*,*c*) Production of TKE versus y^+, where the results from the large-scale simulations display $\mathcal{P}_k^+$ from (4.5), while the model results display the sum of $\mathcal{P}_{k,SG}^+$ from (4.6) and (4.8); (*b*,*d*) Dissipation of TKE versus y^+. For both quantities, the ZPG and APG flows are displayed in panels (*a*,*b*) and (*c*,*d*), respectively. The vertical, black dash–dotted lines mark the beginning of the fringe region $y^+ = 300$.

First, since the mean advection $U^+\partial_x^+\langle k\rangle^+ + V^+\partial_y^+\langle k\rangle^+$ from the large-scale simulations and the slow-growth advection

$$2\epsilon\langle k\rangle^+ U^+ \tag{4.7}$$

from the NWP model cases have a maximum value no larger than 10^{-3}, they are not plotted here.

For the production $\mathcal{P}_{k,SG}$, the inconsistency between the continuity equations (2.17) and (3.8) leads to some 'spurious' $O(\epsilon)$ production terms for the SG-NWP model given by

$$\mathcal{P}_{k,spur}^+ = \epsilon\left(U^+\langle u'u'\rangle^+ + \frac{1}{2}y^+U^+\frac{\partial}{\partial y^+}\langle u'u'\rangle^+\right). \tag{4.8}$$

Figure 11(*a*,*c*) displays $\mathcal{P}_k^+$ from (4.5) for the large-scale simulation cases, and the sum of $\mathcal{P}_{k,SG}^+$ from (4.6) and the spurious production (4.8) for the SG-NWP flows. Note that for the zero and adverse-pressure-gradient flows considered in this work, production is due almost exclusively to the product of $\partial U/\partial y$ and the Reynolds shear stress. For example, this term accounts for approximately 97.5 % of the total production for the three large-scale

flows from table 1. Similarly, the $O(\epsilon)$ terms account for only 0.2 %, 5.7 % and 4.7 % of the SG model's production $\mathcal{P}^+_{k,SG}$ for $y^+ \in [0, 300]$ for SG-NWP-ZPG, SG-NWP-β1 and SG-NWP-β1.7, respectively, while the spurious production (4.8) is no larger than 0.1 %, 3.7 % and 3.4 % of $\mathcal{P}^+_{k,SG}$ for these three model cases.

As expected, there is little difference between the SG-NWP-ZPG and NWP-ZPG production profiles, since the mean velocity gradient and Reynold shear stress profiles for both model flows are nearly identical. Both are in excellent agreement with the SJM-β0 DNS case. For the adverse-pressure-gradient cases, the SG-NWP model's production $\mathcal{P}^+_{k,SG} + \mathcal{P}^+_{k,spur}$ is consistently smaller than the corresponding cases when $\epsilon = 0$. At the near-wall production peak ($y^+ \approx 12$), this results in better agreement with the BVOS-β1.7 case for the SG-NWP model than the $\epsilon = 0$ case, while for the KS-β1 case, the agreement is slightly worse. In both cases, the slow-growth model underpredicts the production profiles from the large-scale simulations for $y^+ \gtrsim 60$, consistent with the results for the mean streamwise velocity gradient.

Unlike the production of turbulent kinetic energy, the dissipation $\varepsilon_k = \nu\langle \partial_j u_i' \partial_j u_i' \rangle$ does not possess any additional slow-growth contributions, as previously noted. Figure 11(*b*,*d*) displays the dissipation profiles for the model and large-scale simulation cases. Although there is no discernible difference between the NWP model with and without slow-growth effects in the zero-pressure-gradient case, they do impact the model dissipation profiles in the adverse-pressure-gradient cases. In particular, they effect a reduction in the maximum dissipation that occurs at the wall, resulting in better agreement with the large-scale simulation values.

Similar to the dissipation, the viscous transport does not possess any $O(\epsilon)$ slow-growth contributions. However, there are indeed some $O(\epsilon)$ 'spurious' contributions to the SG-NWP model's turbulent transport given by

$$T^+_{k,spur} = \epsilon \left(\langle k u' \rangle^+ + y^+ \left\langle k \frac{\partial u'}{\partial y} \right\rangle^+ \right) \tag{4.9}$$

that arise from omitting the $O(\epsilon)$ contribution to the fluctuating continuity equation (2.17). The omission of both this term and the $O(\epsilon)$ pressure term in (2.19) from the SG-NWP model equations also leads to some errors in the pressure transport. In particular, the model's pressure transport does not include any slow-growth contributions, in contrast to $\Upsilon_{k,SG}$, so that in effect there is a spurious contribution given by

$$\Upsilon^+_{k,spur} = -\epsilon \left(3\langle p' u' \rangle^+ + y^+ \frac{\partial}{\partial y^+} \langle p' u' \rangle^+ \right). \tag{4.10}$$

The SG-NWP turbulent $T^+_{k,SG} + T^+_{k,spur}$, pressure $\Upsilon^+_{k,SG} + \Upsilon^+_{k,spur}$ and viscous $D^+_{k,SG}$ transport profiles are displayed in figure 12 and show a reasonable agreement to the corresponding profiles T^+_k, Υ^+_k and D^+_k (as defined in (4.5)) from the large-scale simulations. In particular, the SG-NWP model predicts a lower value of viscous transport at the wall than the corresponding model simulations with $\epsilon = 0$, similar to the dissipation profiles. In contrast, the pressure transport at the wall is notably less accurate when including slow-growth effects. The error is not due to the spurious pressure transport; the spurious terms generally contribute no more than 5 % to the model's total turbulent and pressure transport profiles, similar to the TKE production. Since pressure is generally responsible for enforcing continuity, it is possible that the $O(\epsilon)$ error in the fluctuating SG continuity equation (3.8) is responsible for the relatively large error. It would be useful to test this hypothesis in future work; a reformulation of the velocity-vorticity method due

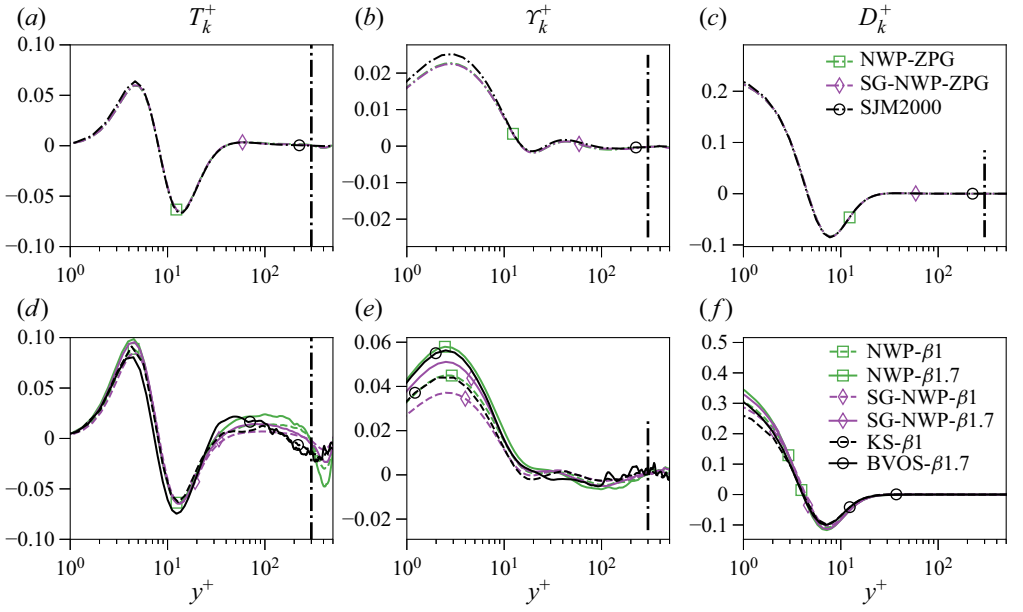

Figure 12. (*a*,*d*) Turbulent, (*b*,*e*) pressure and (*c*,*f*) viscous transport of TKE versus y^+. The results from the large-scale simulations display T_k^+, Υ_k^+ and D_k^+ from (4.5), respectively, while the model results display $T_{k,SG}^+ + T_{k,spur}^+$, $\Upsilon_{k,SG}^+ + \Upsilon_{k,spur}^+$ and D_k^+. The vertical, black dash–dotted lines mark the beginning of the fringe region $y^+ = 300$.

to Kim *et al.* (1987) used here will be required to account for the fact that the velocity fluctuations are not divergence free.

5. Discussion

A primary goal of the SG-NWP model is to understand how pressure gradients affect the small-scale motions in a wall-bounded turbulent flow. The model is formulated by homogenizing a 'real' patch of near-wall turbulence and simulating the result in a restricted domain localized to the wall. The domain is periodic in the streamwise and spanwise directions, similar to the minimal flow unit simulations first conducted by Jiménez & Moin (1991). Within the domain, the pressure gradient is assumed to be constant, while streamwise growth of the mean wall-shear stress that occurs in a turbulent boundary layer, for example, is accounted for asymptotically, similar to the related works by Spalart (1988) and Topalian *et al.* (2017). Far-field boundary conditions in the wall-normal direction are formulated by using a fringe-region (Colonius 2004) in which the mean flux of streamwise momentum in the wall-normal direction is prescribed as a function of the pressure gradient and the asymptotic growth parameter.

Overall, the model simulates only the near-wall small-scale motions. The dynamics of any turbulent structures larger than the NWP model domain size in the stream and/or spanwise direction are approximated only by the evolution of the Fourier modes of the velocity fields with $k_x = 0$ and/or $k_z = 0$. By comparing the model statistics to those generated by a direct numerical simulation that resolves all scales of motion, the relative importance of the large-scale motions can be assessed. The relative importance of streamwise growth of the near-wall region can also be assessed by comparing model cases that include the asymptotic terms (i.e. cases with $\epsilon \neq 0$) to those that do not (cases

with $\epsilon = 0$). The present investigation is hence in a similar spirit to the computational 'experiments' that were recommended and conducted by Jiménez & Pinelli (1999).

To this end, several conclusions can be drawn from the results presented in § 4. First, the mean velocity profile can be accurately computed for $y^+ \in [0, 300]$ (to within approximately 6 %) without resolving the large-scale structures. This accuracy is insensitive to whether asymptotic growth effects are included or not. The Reynolds shear stress profiles can also be accurately computed (up to an error of approximately 9 %) without resolving the large-scale structures. The accuracy greatly deteriorates if growth effects are not accounted for (especially for $y^+ \gtrsim 20$), however, highlighting the effect that the spatial development of the mean wall-shear has on the near-wall stress balance in adverse-pressure-gradient flows. Similar conclusions can be drawn for the wall-normal velocity variance. In contrast, the SG-NWP model cannot accurately compute the stream and spanwise velocity variance statistics, as the modulation and superposition effects known to be present in channel flows, zero-pressure gradient TBLs and adverse-pressure-gradient TBLs are simply not represented in the model.

Another important conclusion concerns the universality of small-scale motions in the near-wall region. It is well established for channel flows and zero-pressure-gradient boundary layers that the viscous-scaled TKE associated with small-scale motions is independent of Re_τ (Samie *et al.* 2018; Lee & Moser 2019; Carney *et al.* 2020; Wang *et al.* 2021*b*). The results here strongly suggest that for flows with adverse pressure gradients, small-scale universality in the near-wall region should be pressure gradient dependent. The SG-NWP model's high-pass filtered, viscous-scaled TKE increased with the strength of the applied adverse pressure gradient. It is natural to speculate that universality might be recovered if the small-scale TKE is instead scaled in so-called pressure-viscous units (Gungor *et al.* 2016), the non-dimensionalization based on the kinematic viscosity ν and $u_{pi} := (\nu/\rho(\mathrm{d}P/\mathrm{d}x))^{1/3}$. This was not the case, however, in our numerical tests (not shown). Consequently, the generalization to adverse-pressure-gradient flows of the 'universal signal' constructed by Mathis *et al.* (2011) for zero-pressure gradient flows ought to depend on the APG strength.

The current modelling approach of simulating only the small-scale motions is, in a sense, the reciprocal of what is done in large eddy simulations, where only the large scales are simulated, and the small-scales are approximated with a subgrid model. It is thus natural to try and link the SG-NWP model to an LES. As a quantitative model of near-wall turbulence, the SG-NWP model defines a two-parameter family of near-wall turbulent flows, parameterized by the imposed pressure gradient $\mathrm{d}P^+/\mathrm{d}x^+$ and the growth parameter ϵ. For such an application, one would invoke the scale-separation assumption discussed in § 2.1 and use SG-NWP flows matched to the local pressure gradient and growth parameter associated with the large-scale, outer-layer flow simulated by the LES. The coupling could be formulated sequentially (i.e. by precomputing a library of input and output responses) or concurrently (i.e. 'on the fly') (Abdulle *et al.* 2012). See the works of Sandham, Johnstone & Jacobs (2017), Wang, Huang & Xu (2021*a*), Elnahhas, Lozano-Durán & Moin (2021) and Chen & He (2022) for examples of the latter.

Finally, as mentioned in the fundamental modelling assumptions discussed in § 2.1, the SG-NWP modelling approach necessarily breaks down when the 'real' flow to be modelled approaches separation, i.e. as $u_\tau \to 0$. The model is currently formulated to operate in viscous units; the forcing function f in the fringe region ensures the model's wall shear stress at equilibrium equals unity. The strength of the forcing increases with ϵ and $\mathrm{d}P^+/\mathrm{d}x^+$, however, both of which blow up as $u_\tau \to 0$. Hence, an alternative scaling will be needed to improve on the current approach to model flows sufficiently close to separation.

One starting point for future research may be to revisit the study by Nickels (2004) using data from recent large-scale DNS and WRLES of separated flows, e.g. Hickel & Adams (2008), Gungor *et al.* (2016).

6. Conclusions

The slow-growth (SG) model described here was formulated to extend the near-wall patch (NWP) representation of wall-turbulence presented by Carney *et al.* (2020) to flows with non-negligible streamwise development of mean quantities. A primary objective is to provide a computationally accessible quantitative model of wall-turbulence for such situations, for example, in boundary layers with adverse pressure gradients. Another is to characterize the extent to which the dynamics of the small-scale motions, isolated from modulations by large-scale structures, are responsible for observed characteristics of near-wall turbulence. As in Spalart (1988) and Topalian *et al.* (2017), the model equations of motion are informed by asymptotic analysis of the Navier–Stokes (NS) equations; the fundamental assumption in the current setting is a separation between the viscous length scale and the length scale over which the mean wall shear stress evolves.

Because the SG-NWP model domain size scales in viscous units, the simulations require orders of magnitude fewer computational resources compared with large-scale DNS and wall-resolved LES. For example, the model's computational grid is approximately a factor of 5700 and 1000 smaller than the DNS calculations of Sillero *et al.* (2013) and Kitsios *et al.* (2017), respectively, and a factor of approximately 144 smaller than the wall-resolved LES of Bobke *et al.* (2017).

The SG-NWP model could hence be deployed as a vehicle for relatively inexpensive numerical 'experiments' on near-wall dynamics influenced by pressure gradients. For example, the model could be used to study the interactions of the near-wall, small-scale dynamics with such complications as heat transfer, turbophoresis or chemical reactions. The model should be particularly well suited for investigating the effects of surface roughness on the near-wall region.

Finally, although the separation of scales on which the SG model is based is well founded for a variety of practically relevant flows, it is important to keep in mind that it is still limited to a range of pressure gradients that are not too large when scaled in viscous units. Because the viscous length scale changes more rapidly with stronger adverse pressure gradients, the asymptotic analysis on which the model is founded will no longer be valid. In particular, this makes the model inadequate to describe near-wall flow near a point of boundary layer separation.

Acknowledgements. The research used the computing resources of the Texas Advanced Computing Center (TACC) at The University of Texas at Austin. The authors are grateful to both C. Atkinson and R. Vineusa for sharing the statistics from large-scale adverse-pressure-gradient simulations. The authors thank G. Yalla and B. Engquist for insightful discussions, as well as P. Mohan for helpful suggestions regarding time integration of the equations of motion. Lastly, the authors thank the referees for their many helpful suggestions that significantly improved the manuscript.

Funding. The work presented here was supported by the National Science Foundation (Award No. 1904826), as well as by the Oden Institute for Computational Engineering and Sciences.

Declaration of interests. The authors report no conflicts of interest.

Author ORCIDs.
Sean P. Carney https://orcid.org/0000-0001-9644-3727;
Robert D. Moser https://orcid.org/0000-0001-7735-1253.

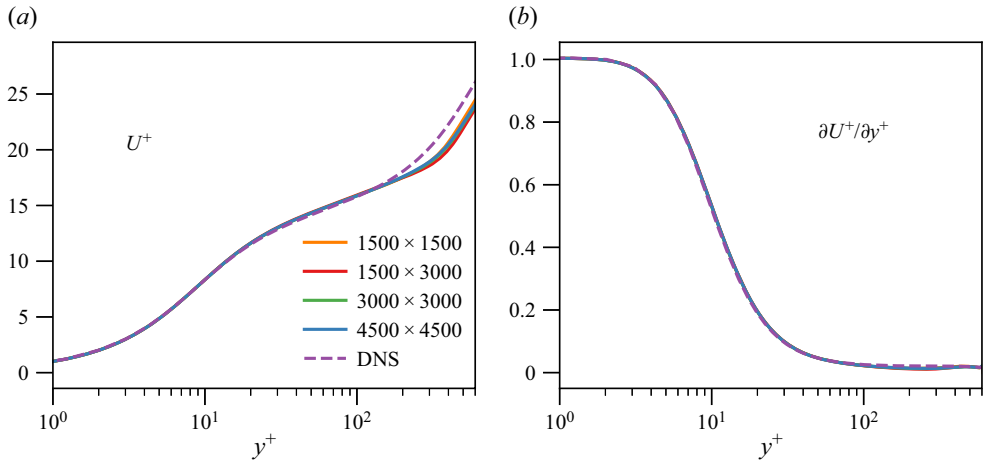

Figure 13. Mean velocity and mean velocity gradient profiles versus y^+ for the DNS adverse-pressure-gradient simulation KS-β1 and SG-NWP-β1 model cases with various domain sizes $L_x^+ \times L_z^+$.

Appendix. Effect of wall-parallel domain size on statistical quantities

A number of simulations were conducted at fixed values of $\mathrm{d}P^+/\mathrm{d}x^+$ and ϵ that correspond to the model case SG-NWP-β1 from table 2 to assess the sensitivity of the model's statistics to the size of the near-wall patch domain size in the stream and spanwise directions. In particular, simulations were conducted with $L_x^+ \times L_z^+ = 1500 \times 1500$ (as listed in table 3), as well as with 1500×3000, 3000×3000 and 4500×4500. In each case, the number of Fourier modes N_x and N_z were increased proportionally to maintain the resolution Δx^+ and Δz^+ listed in table 3.

Figures 13 and 14 show the mean velocity, the mean velocity derivative and the Reynolds stress terms for each domain size case, as well as the DNS profiles from Kitsios *et al.* (2017). The mean velocity, its derivative and the Reynolds shear stress $\langle u'v' \rangle$ all exhibit only slight variations as a function of the domain size. The wall-normal variances show a small increase with increasing L_x^+ and L_z^+, but the difference is less than a few percent. The turbulent kinetic energy budget terms (not shown) are also either unaffected or show slight trends comparable to that of the wall-normal velocity variance.

In contrast, the streamwise velocity variances show a mild decrease with increasing domain size, while the spanwise velocity variances show a non-trival increase. As mentioned in § 3.3, the differences can be attributed to the fact that the NWP includes more large-scale structures as L_x^+ and L_z^+ increase. At even larger domain sizes, the NWP size will begin to approach that of the full DNS; for example, at $L_z^+ \geq 3000$, the NWP spanwise domain length is at least a third of that of the DNS, owing to the relatively low Re_τ at which it was conducted. In the limit as the NWP stream and spanwise domain sizes approach that of the DNS, it is reasonable to expect the NWP velocity variances to convergence to some limiting profiles. However, these limits need not correspond to the DNS statistics, since the two flows are fundamentally different in multiple aspects. For example, they differ in the wall-normal domain size, the boundary conditions at $y = L_y$ and the use of a fringe region in the NWP. Another important difference is the treatment of boundary conditions in the stream and spanwise directions; the DNS uses periodic conditions and a recycling technique to account for boundary layer growth, while the NWP uses slow-growth asymptotics to account for streamwise growth in the near-wall region.

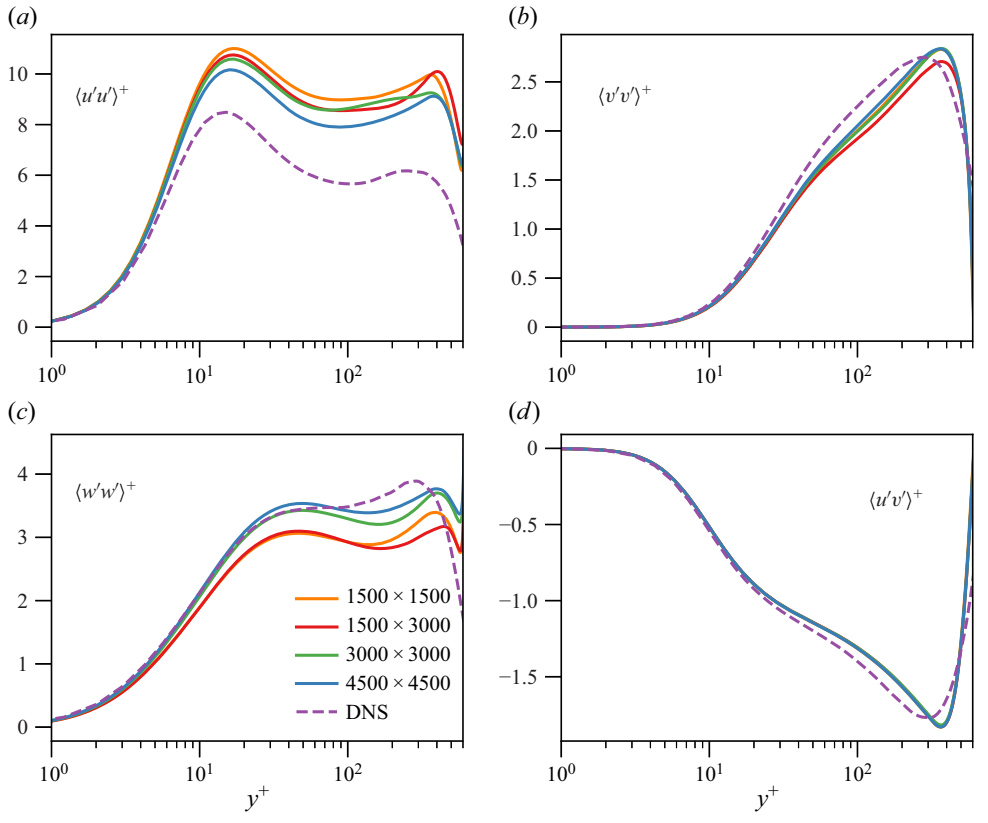

Figure 14. Reynolds stress profiles versus y^+ for the DNS adverse-pressure-gradient simulation KS-β1 and SG-NWP-β1 model cases with various domain sizes $L_x^+ \times L_z^+$.

References

Abdulle, A., Ee, W., Engquist, B. & Vanden-Eijnden, E. 2012 The heterogeneous multiscale method. *Acta Numerica* **21**, 1–87.

Araya, G., Castillo, L., Meneveau, C. & Jansen, K. 2011 A dynamic multi-scale approach for turbulent inflow boundary conditions in spatially developing flows. *J. Fluid Mech.* **670**, 581–605.

Bobke, A., Vinuesa, R., Örlü, R. & Schlatter, P. 2017 History effects and near equilibrium in adverse-pressure-gradient turbulent boundary layers. *J. Fluid Mech.* **820**, 667–692.

Bose, S.T. & Park, G.I. 2018 Wall-modeled large-eddy simulation for complex turbulent flows. *Annu. Rev. Fluid Mech.* **50** (1), 535–561.

Bradshaw, P. 1967 The turbulence structure of equilibrium boundary layers. *J. Fluid Mech.* **29** (4), 625–645.

Carney, S.P., Engquist, B. & Moser, R.D. 2020 Near-wall patch representation of wall-bounded turbulence. *J. Fluid Mech.* **903**, A23.

Chen, C. & He, L. 2022 On locally embedded two-scale solution for wall-bounded turbulent flows. *J. Fluid Mech.* **933**, A47.

Chernyshenko, S. 2021 Extension of QSQH theory of scale interaction in near-wall turbulence to all velocity components. *J. Fluid Mech.* **916**, A52.

Clauser, F.H. 1954 Turbulent boundary layers in adverse pressure gradients. *J. Aeronaut. Sci.* **21** (2), 91–108.

Colonius, T. 2004 Modeling artificial boundary conditions for compressible flow. *Annu. Rev. Fluid Mech.* **36**, 315–345.

DeGraaff, D.B. & Eaton, J.K. 2000 Reynolds-number scaling of the flat-plate turbulent boundary layer. *J. Fluid Mech.* **422**, 319–346.

Elnahhas, A., Lozano-Durán, A. & Moin, P. 2021 Toward a flow-structure-based wall-modeled large-eddy simulation paradigm. arXiv:2101.00528.

GANAPATHISUBRAMANI, B., HUTCHINS, N., MONTY, J.P., CHUNG, D. & MARUSIC, I. 2012 Amplitude and frequency modulation in wall turbulence. *J. Fluid Mech.* **712**, 61–91.

GUARINI, S.E., MOSER, R.D., SHARIFF, K. & WRAY, A. 2000 Direct numerical simulation of a supersonic turbulent boundary layer at Mach 2.5. *J. Fluid Mech.* **414**, 1–33.

GUNGOR, A.G., MACIEL, Y., SIMENS, M.P. & SORIA, J. 2016 Scaling and statistics of large-defect adverse pressure gradient turbulent boundary layers. *Intl J. Heat Fluid Flow* **59**, 109–124.

HAMILTON, J.M., KIM, J. & WALEFFE, F. 1995 Regeneration mechanisms of near-wall turbulence structures. *J. Fluid Mech.* **287**, 317–348.

HARUN, Z., MONTY, J.P., MATHIS, R. & MARUSIC, I. 2013 Pressure gradient effects on the large-scale structure of turbulent boundary layers. *J. Fluid Mech.* **715**, 477–498.

HICKEL, S. & ADAMS, N.A. 2008 Implicit LES applied to zero-pressure-gradient and adverse-pressure-gradient boundary-layer turbulence. *Intl J. Heat Fluid Flow* **29** (3), 626–639.

HOSSEINI, S.M., VINUESA, R., SCHLATTER, P., HANIFI, A. & HENNINGSON, D.S. 2016 Direct numerical simulation of the flow around a wing section at moderate Reynolds number. *Intl J. Heat Fluid Flow* **61**, 117–128.

HUTCHINS, N. & MARUSIC, I. 2007 Large-scale influences in near-wall turbulence. *Phil. Trans. R. Soc. A: Math. Phys. Engng Sci.* **365**, 647–664.

INOUE, M., PULLIN, D.I., HARUN, Z. & MARUSIC, I. 2013 LES of the adverse-pressure gradient turbulent boundary layer. *Intl J. Heat Fluid Flow* **44**, 293–300.

JEONG, J., HUSSAIN, F., SCHOPPA, W. & KIM, J. 1997 Coherent structures near the wall in a turbulent channel flow. *J. Fluid Mech.* **332**, 185–214.

JIMÉNEZ, J. & MOIN, P. 1991 The minimal flow unit in near-wall turbulence. *J. Fluid Mech.* **225**, 213–240.

JIMÉNEZ, J. & PINELLI, A. 1999 The autonomous cycle of near-wall turbulence. *J. Fluid Mech.* **389**, 335–359.

KIM, J., MOIN, P. & MOSER, R. 1987 Turbulence statistics in fully developed channel flow at low Reynolds number. *J. Fluid Mech.* **177**, 133–166.

KITSIOS, V., SEKIMOTO, A., ATKINSON, C., SILLERO, J.A., BORRELL, G., GUNGOR, A.G., JIMÉNEZ, J. & SORIA, J. 2017 Direct numerical simulation of a self-similar adverse pressure gradient turbulent boundary layer at the verge of separation. *J. Fluid Mech.* **829**, 392–419.

KNOPP, T., BUCHMANN, N.A., SCHANZ, D., EISFELD, B., CIERPKA, C., HAIN, R., SCHRÖDER, A. & KÄHLER, C.J. 2015 Investigation of scaling laws in a turbulent boundary layer flow with adverse pressure gradient using PIV. *J. Turbul.* **16** (3), 250–272.

KNOPP, T., NOVARA, M., SCHULEIN, E., SCHANZ, D., SCHRODER, A., REUTHER, N. & KAHLER, C.J. 2017 Investigation of a turbulent boundary layer flow at high Reynolds number using particle-imaging and implications for RANS modeling. In *Tenth International Symposium on Turbulence and Shear Flow Phenomena*. Begel House.

LEE, M. 2015 Direct numerical simulation (DNS) for incompressible turbulent channel flow at $Re_\tau = 5200$. PhD thesis, The University of Texas at Austin.

LEE, J.H. 2017 Large-scale motions in turbulent boundary layers subjected to adverse pressure gradients. *J. Fluid Mech.* **810**, 323–361.

LEE, M., MALAYA, N. & MOSER, R.D. 2013 Petascale direct numerical simulation of turbulent channel flow on up to 786 K cores. In *the International Conference for High Performance Computing, Networking, Storage and Analysis*, pp. 1–11. ACM Press.

LEE, M. & MOSER, R.D. 2015 Direct numerical simulation of turbulent channel flow up to $Re_\tau = 5200$. *J. Fluid Mech.* **774**, 395–415.

LEE, M. & MOSER, R.D. 2017 Large-scale motions in turbulent Poiseuille & Couette flows. In *Tenth International Symposium on Turbulence and Shear Flow Phenomena*.

LEE, M. & MOSER, R.D. 2019 Spectral analysis of the budget equation in turbulent channel flows at high Reynolds number. *J. Fluid Mech.* **860**, 886–938.

LEE, J.-H. & SUNG, H.J. 2009 Structures in turbulent boundary layers subjected to adverse pressure gradients. *J. Fluid Mech.* **639**, 101–131.

LEE, M., ULERICH, R., MALAYA, N. & MOSER, R.D. 2014 Experiences from leadership computing in simulations of turbulent fluid flows. *Comput. Sci. Engng* **16** (5), 24–31.

LUND, T.S., WU, X. & SQUIRES, K.D. 1998 Generation of turbulent inflow data for spatially-developing boundary layer simulations. *J. Comput. Phys.* **140** (2), 233–258.

MAEDER, T., ADAMS, N.A. & KLEISER, L. 2001 Direct simulation of turbulent supersonic boundary layers by an extended temporal approach. *J. Fluid Mech.* **429**, 187–216.

MARQUILLIE, M., LAVAL, J.-P. & DOLGANOV, R. 2008 Direct numerical simulation of a separated channel flow with a smooth profile. *J. Turbul.* **9**, N1.

MARUSIC, I., MATHIS, R. & HUTCHINS, N. 2010*a* High Reynolds number effects in wall turbulence. *Intl J. Heat Fluid Flow* **31** (3), 418–428.

MARUSIC, I., MATHIS, R. & HUTCHINS, N. 2010*b* Predictive model for wall-bounded turbulent flow. *Science* **329** (5988), 193–196.

MATHIS, R., HUTCHINS, N. & MARUSIC, I. 2011 A predictive inner–outer model for streamwise turbulence statistics in wall-bounded flows. *J. Fluid Mech.* **681**, 537–566.

MIZUNO, Y. & JIMÉNEZ, J. 2013 Wall turbulence without walls. *J. Fluid Mech.* **723**, 429–455.

NA, Y. & MOIN, P. 1998 Direct numerical simulation of a separated turbulent boundary layer. *J. Fluid Mech.* **374**, 379–405.

NICKELS, T.B. 2004 Inner scaling for wall-bounded flows subject to large pressure gradients. *J. Fluid Mech.* **521**, 217–239.

OLIVER, T.A., MALAYA, N., ULERICH, R. & MOSER, R.D. 2014 Estimating uncertainties in statistics computed from direct numerical simulation. *Phys. Fluids* **26**, 035101.

PIOMELLI, U. & BALARAS, E. 2002 Wall-layer models for large-eddy simulations. *Annu. Rev. Fluid Mech.* **34** (1), 349–374.

POZUELO, R., LI, Q., SCHLATTER, P. & VINUESA, R. 2022 An adverse-pressure-gradient turbulent boundary layer with nearly constant $\beta \simeq 1.4$ up to $Re_\theta \simeq 8700$. *J. Fluid Mech.* **939**, A34.

RAHGOZAR, S. & MACIEL, Y. 2012 Statistical analysis of low-and high-speed large-scale structures in the outer region of an adverse pressure gradient turbulent boundary layer. *J. Turbul.* **13**, N46.

ROMERO, S., ZIMMERMAN, S., PHILIP, J., WHITE, C. & KLEWICKI, J. 2022 Properties of the inertial sublayer in adverse pressure-gradient turbulent boundary layers. *J. Fluid Mech.* **937**, A30.

SAMIE, M., MARUSIC, I., HUTCHINS, N., FU, M.K., FAN, Y., HULTMARK, M. & SMITS, A.J. 2018 Fully resolved measurements of turbulent boundary layer flows up to $Re_\tau = 20\,000$. *J. Fluid Mech.* **851**, 391–415.

SANDHAM, N.D., JOHNSTONE, R. & JACOBS, C.T. 2017 Surface-sampled simulations of turbulent flow at high Reynolds number. *Intl J. Numer. Meth. Fluids* **85** (9), 525–537.

SANMIGUEL VILA, C., ÖRLÜ, R., VINUESA, R., SCHLATTER, P., IANIRO, A. & DISCETTI, S. 2017 Adverse-pressure-gradient effects on turbulent boundary layers: statistics and flow-field organization. *Flow Turbul. Combust.* **99** (3), 589–612.

SANMIGUEL VILA, C., VINUESA, R., DISCETTI, S., IANIRO, A., SCHLATTER, P. & ÖRLÜ, R. 2020 Separating adverse-pressure-gradient and Reynolds-number effects in turbulent boundary layers. *Phys. Rev. Fluids* **5** (6), 064609.

SATO, M., ASADA, K., NONOMURA, T., KAWAI, S. & FUJII, K. 2017 Large-eddy simulation of NACA 0015 airfoil flow at Reynolds number of 1.6×106. *AIAA J.* **55** (2), 673–679.

SAVITZKY, A. & GOLAY, M.J.E. 1964 Smoothing and differentiation of data by simplified least squares procedures. *Analyt. Chem.* **36** (8), 1627–1639.

SILLERO, J.A., JIMÉNEZ, J. & MOSER, R.D. 2013 One-point statistics for turbulent wall-bounded flows at Reynolds numbers up to $\delta^+ \approx 2000$. *Phys. Fluids* **25** (10), 105102.

SKOTE, M. & HENNINGSON, D.S. 2002 Direct numerical simulation of a separated turbulent boundary layer. *J. Fluid Mech.* **471**, 107–136.

SMITS, A. & MARUSIC, I. 2013 Wall-bounded turbulence. *Phys. Today* **66** (9), 25.

SMITS, A.J., MCKEON, B.J. & MARUSIC, I. 2011 High-Reynolds number wall turbulence. *Annu. Rev. Fluid Mech.* **43**, 353–375.

SPALART, P.R. 1988 Direct simulation of a turbulent boundary layer up to $Re_\theta = 1410$. *J. Fluid Mech.* **187**, 61–98.

SPALART, P.R. & LEONARD, A. 1987 Direct numerical simulation of equilibrium turbulent boundary layers. In *Turbulent Shear Flows 5* (ed. F. Durst, B.E. Launder, J.L. Lumley, F.W. Schmidt & J.H. Whitelaw), pp. 234–252. Springer.

SPALART, P.R., MOSER, R.D. & ROGERS, M.M. 1991 Spectral methods for the Navier–Stokes equations with one infinite and two periodic directions. *J. Comput. Phys.* **96**, 297–324.

SPALART, P.R. & WATMUFF, J.H. 1993 Experimental and numerical study of a turbulent boundary layer with pressure gradients. *J. Fluid Mech.* **249**, 337–371.

TANARRO, Á., VINUESA, R. & SCHLATTER, P. 2020 Effect of adverse pressure gradients on turbulent wing boundary layers. *J. Fluid Mech.* **883**, A8.

TOPALIAN, V., OLIVER, T.A., ULERICH, R. & MOSER, R.D. 2017 Temporal slow-growth formulation for direct numerical simulation of compressible wall-bounded flows. *Phys. Rev. Fluids* **2** (8), 084602.

WANG, L., HU, R. & ZHENG, X. 2021*b* A scaling improved inner–outer decomposition of near-wall turbulent motions. *Phys. Fluids* **33** (4), 045120.

WANG, H.-N., HUANG, W.-X. & XU, C.-X. 2021*a* Synthetic near-wall small-scale turbulence and its application in wall-modeled large-eddy simulation. *Phys. Fluids* **33** (9), 095102.

YOON, M., HWANG, J. & SUNG, H.J. 2018 Contribution of large-scale motions to the skin friction in a moderate adverse pressure gradient turbulent boundary layer. *J. Fluid Mech.* **848**, 288–311.

ZHANG, C. & CHERNYSHENKO, S.I. 2016 Quasisteady quasihomogeneous description of the scale interactions in near-wall turbulence. *Phys. Rev. Fluids* **1** (1), 014401.